A&A 397, 693–710 (2003)
DOI: 10.1051/0004-6361:20021545

Astronomy & Astrophysics

Near-IR echelle spectroscopy of Class I protostars: Mapping Forbidden Emission-Line (FEL) regions in [FeII]

C. J. Davis[1], E. Whelan[2], T. P. Ray[2], and A. Chrysostomou[3]

[1] Joint Astronomy Centre, 660 North A'ohōkū Place, University Park, Hilo, Hawaii 96720, USA
[2] Dublin Institute for Advanced Studies, School of Cosmic Physics, 5 Merrion Square, Dublin 2, Ireland
[3] Department of Physical Sciences, University of Hertfordshire, Hatfield, Herts AL10 9AB, UK

Received 27 August 2002 / Accepted 22 October 2002

Abstract. Near-IR echelle spectra in [FeII] 1.644 μm emission trace Forbidden Emission Line (FEL) regions towards seven Class I HH energy sources (SVS 13, B5-IRS1, IRAS 04239+2436, L1551-IRS5, HH 34-IRS, HH 72-IRS and HH 379-IRS) and three classical T Tauri stars (AS 353A, DG Tau and RW Aur). The parameters of these FEL regions are compared to the characteristics of the Molecular Hydrogen Emission Line (MHEL) regions recently discovered towards the same outflow sources (Davis et al. 2001 – Paper I). The [FeII] and H_2 lines both trace emission from the base of a large-scale collimated outflow, although they clearly trace different flow components. We find that the [FeII] is associated with higher-velocity gas than the H_2, and that the [FeII] emission peaks further away from the embedded source in each system. This is probably because the [FeII] is more closely associated with HH-type shocks in the inner, on-axis jet regions, while the H_2 may be excited along the boundary between the jet and the near-stationary, dense ambient medium that envelopes the protostar. Indeed, there is spatial and kinematic evidence that [FeII] and the more typically-used optical emission lines, the red [SII] doublet, do trace almost the same shock-excited regions in HH jets and FEL regions alike.

Key words. ISM: jets and outflows – stars: pre-main-sequence – ISM: Herbig-Haro objects

1. Introduction

Comparitively little is known about Herbig-Haro (HH) jets and molecular outflows close to their protostellar driving sources. Optical forbidden-line emission from the base of HH jets from classical T Tauri stars (CTTS) has been studied with high-resolution imaging (HST and ground-based AO) and spectroscopic techniques (e.g. Ray et al. 1996; Bacciotti et al. 2000; Dougados et al. 2000; Hirth et al. 1994, 1997; Takami et al. 2001; Woitas et al. 2002), yet only recently have observations yielded information on the same regions in molecular outflows from more deeply embedded protostars (Davis et al. 2001 – hereafter referred to as Paper I; Davis et al. 2002). The recent discovery of "Molecular Hydrogen Emission Line (MHEL)" regions in Class I young stellar objects (YSOs) is of considerable interest, since the survival of H_2 in the inner jet regions constrains models of HH jet acceleration, collimation and evolution within a few hundred AU of these very young outflow sources.

The H_2 echelle observations presented in Paper I reveal complex, low and high-velocity molecular line emission almost coincident with each Class I source. The characteristics of these MHEL regions are much like those of the "Forbidden Emission Line (FEL)" regions observed in CTTSs (e.g. Hirth et al. 1997), even though the optical lines and near-IR H_2 lines trace very different excitation conditions. In both MHELs and FELs: *i)* multiple (low and high) velocity components are observed; *ii)* the emission regions are generally offset from the source, along the blue-shifted flow axis, by a few tens to a few hundred AU; and *iii)* the higher-velocity gas is always slightly further offset than the slower gas. Indeed, even though molecular hydrogen is dissociated under extreme excitation conditions, radial H_2 velocities approaching 50–150 km s^{-1} are observed in some MHEL regions.

To further investigate the relationship between MHEL and FEL regions, we now present spectroscopic observations made in [FeII] at 1.644 μm. The same Class I sources observed in H_2 at 2.122 μm (apart from GGD 27), as well as three CTTSs (Class II sources) known to possess optical FEL regions and HH jets, have been observed in [FeII] emission. [FeII] is a useful tracer of intermediate/high-excitation shocks in HH objects and molecular outflows. Much like the optical forbidden lines from, e.g. [OI], [SII], [NII], etc., the near-IR [FeII] lines can be used to complement H_2 observations (e.g. Reipurth et al. 2000). In outflows the shock-excited H_2 emission derives from dense (10^4 cm^{-3}), warm (~2000 K) molecular gas, while the metastable transitions of species like [FeII] dominate the cooling at similar densities though higher temperatures, of the order of 10^4 K (Hollenbach & McKee 1989). Hamann et al. (1994) have used H-band [FeII] lines to probe FEL regions in

Send offprint requests to: C. J. Davis,
e-mail: c.davis@jach.hawaii.edu

Table 1. Observing log: the top seven targets are Class I YSOs; the bottom three are T Tauri stars.

Source	RA (2000.0)	Dec (2000.0)	[1]Slit PA	[2]Exp. Time (min)
SVS 13	03 29 03.7	+31 16 02	123°	40
B5-IRS1	03 47 41.6	+32 51 46	73°	33
IRAS 04239+2436	04 26 56.4	+24 43 36	[3]59°	40
L1551-IRS5	04 31 33.6	+18 08 11	66°	33
HH 34-IRS	05 35 29.8	−06 26 58	167°	33
HH 72-IRS	07 20 08.4	−24 02 23	90°	40
HH 379-IRS	21 45 08.2	+47 33 07	82°	40
DG Tau	04 27 04.7	+26 06 17	46°	40
RW Aur	05 07 49.6	+30 24 05	125°	33
AS 353A	19 20 31.0	+11 01 55	106°	40

[1] Slit position angle (east of north).
[2] Total on-source exposure time.
[3] A PA of 45° was used in Paper I for our H_2 observations of IRAS 04239+2436. This new angle was measured from the HST images of Reipurth et al. (2000).

a handful of T Tauri stars. The same [FeII] lines should therefore be a good tracer of the FEL regions associated with Class I YSOs, where optical observations will be hampered by extinction.

2. Observations

Echelle spectra were obtained at the U.K. Infrared Telescope (*UKIRT*) on 1–3 November 2001 UT using the facility 1–5 μm spectrometer CGS 4 (Mountain et al. 1990). Observations in the $a^4D_{7/2} - a^4F_{9/2}$ transition of [FeII] at $\lambda_{\rm vac} = 1.643998\ \mu$m (Johansson 1978) were acquired towards seven Class I sources and three Class II (T Tauri) stars (listed in Table 1). CGS 4 is equipped with a 256 × 256 pixel InSb array; the pixel scale at 1.64 μm measures 0.″41 × 0.″88 (0.″41 in the dispersion direction). A 2-pixel-wide slit was used, resulting in a velocity scale of ∼8.0 km s^{-1} per pixel. The instrumental profile in the dispersion direction, measured from Gaussian fits to arc lines, was 19.0(±1.0) km s^{-1}. For each target the spectrometer slit was orientated along the outflow or HH jet axis, as defined by published, large-scale images of each system (the same slit position angles as in Paper I were used, except for IRAS 04239+2436 where a revised angle was employed based on newly published data).

A sequence, comprising one sky followed by three object exposures was repeated a number of times for each source to build up signal-to-noise, the sky position being typically 30″–60″ away from the source (in a direction orthogonal to the flow axis). Each spectral image was bias subtracted and flat-fielded. Sky-subtracted object frames were then co-added into reduced "groups" (one group frame per target). To wavelength-calibrate these group images, argon and krypton arc lamp spectra were observed just prior to observing each source (and each standard star). The combined lamp spectral images yielded six lines, spread across the dispersion axis, that could be used for accurate wavelength calibration. The argon and krypton lines at $\lambda_{\rm vac}$ = 1.644107 μm and 1.647035 μm were observed directly (in the 33rd order) while lines at 1.694521 μm and 1.599386 μm (argon) and 1.670137 μm and 1.694043 μm (krypton) were detected from adjacent (32nd or 34th) orders. The rest wavelength of [FeII] also lies close to the bright OH sky line, OH(5,3)R_1(2) at 1.64421 μm (Maihara et al. 1993); the separation between the [FeII] and OH lines is only 39 km s^{-1}, or about 5 pixels. This sky-line did not subtract out perfectly in some cases, although because the line is narrow and extended along the full length of the slit (along whole columns), it was easily distinguished from the [FeII] emission associated with each outflow. In these cases, the line was fitted and removed from the spectral image. Before doing this, however, we used it to check the wavelength and subsequent velocity calibration (described below).

Routines available through Starlink were used to identify arc lines and wavelength-calibrate each spectral image, row-by-row. In this way we could also correct for curvature along the slit (spatial) axis in each image. The arc spectral images were first "self-calibrated" so that we could check for variations in the absolute wavelength calibration along the slit axis (along columns); these variations were found to be small, of the order of 5 km s^{-1} towards the edges of the array, and a factor of 2 better within the central 30% of the array where the [FeII] emission was observed. Instrument flexure over the duration of the observations could, however, introduce additional uncertainties in the *absolute* velocity calibration, i.e. by shifting the individual frames with respect to the wavelength reference used to calibrate the reduced group spectral image. By comparing the positions of sky lines in a number of raw frames we found that this effect was also small; indeed, the narrowness of the [FeII] lines and/or residual sky lines in the combined group data for each source (as compared to the instrumental profile width, which is measured from just one frame) confirms this finding. We therefore conclude that the overall velocity calibration is accurate to better than 6 km s^{-1}, while perceived velocity shifts between adjacent spectra observed along the same slit will be more accurate, to within 2–3 km s^{-1}.

Finally, bright G- or K-type giant or main-sequence stars were observed with the same instrumental configuration prior to each outflow source. Narrow telluric absorption features were evident at 1.6429 μm and 1.6455 μm in these data, lines which are displaced by ∼200 km s^{-1} and ∼220 km s^{-1} from the rest wavelength of the target [FeII] line. Some of the standard star spectra also possessed photospheric absorption features (from permitted FeI or other species) at 1.6427 μm, 1.6437 μm, 1.6444 μm and 1.6454 μm. These absorption lines were narrow (≤25 km s^{-1}), so we were able to "patch" across them by interpolating between the continuum on either side of the line, before the standard star spectra were used to flux calibrate the extracted 1D source spectra.

3. Results

Our goal was to use [FeII] to trace FEL regions in the Class I YSOs where MHELs had already been observed. We therefore observed each target from Paper I (except GGD 27) using the same slit position angle (PA) and slit width, so that we could directly compare the H_2 and [FeII] characteristics. In [FeII] we also observed three T Tauri stars. One of these, AS 353A, was observed in H_2 in Paper I: the other two CTTSs have known FEL regions from published optical observations. With these CTTS data we can compare the optical and near-IR characteristics of the FELs, as traced in [SII] and [FeII] respectively. Note that shock models and observations of HH objects do indicate that [FeII] and [SII] trace similar post-shock regions (Hollenbach & McKee 1989; Hamann et al. 1994), even though the [FeII] 1.64 μm line has a higher critical density for collisional excitation than the [SII]$\lambda 6716/\lambda 6731$ lines (3×10^4 cm^{-3} as compared to 2×10^3 cm^{-3} for [SII]). The electron temperature in an [SII]-bright region is expected to be $\geq$13 000 K, while the Fe^+ ionisation fraction is predicted to peak at temperatures of approximately 14 000 K (Hamann 1994); these temperature limits are not strongly dependent on the density (they were calculated for $n_H = 10^5$ cm^{-3}).

[FeII] position-velocity ($P-V$) diagrams for the seven Class I YSOs are shown in Fig. 1; the data obtained for the T Tauri stars are presented in Fig. 2. Where the FEL emission is obscured by strong continuum emission, we also show *continuum-subtracted* $P-V$ diagrams, in Fig. 3. In these plots the continuum emission on either side of the line emission has been fitted, row by row, with a 3rd order polynomial. The fits are then subtracted to leave only the line emission associated with each target.

From the $P-V$ diagrams we also measure the relative positions of the FEL components with respect to the source continuum position. This is done by fitting Gaussians to profiles taken perpendicular to the dispersion direction. For each column in a given $P-V$ diagram (i.e. at each velocity) a measurement of the position of the line emission or the continuum emission is made (line emission positions are obtained from the continuum-subtracted $P-V$ diagrams). These are then plotted against velocity in Fig. 4. Because our spatial resolution along the slit is relatively poor with respect to the seeing, for error bars on the line emission positions (the boxes in Fig. 4) we use the Full Width Half Maximum (*FWHM*) of the Gaussian fits divided by $\sqrt{(}N-1)$, where N is the number of points across the profile ($= 2\times FWHM/0.88''$). The same technique was used in Paper I, where offsets of the MHEL components were presented (although note that the seeing was much better during the H_2 observations). The position of the source continuum is known much more accurately and is indicated in each plot by a polynomial fit to the source continuum positions. The scatter in these continuum points about the fit is an indication of the accuracy with which the continuum position is known; this scatter is of course directly related to the strength of the continuum emission.

Spectra, representing in all cases the sum of 3 rows (equivalent to an on-source area of $\sim 0.8'' \times 2.7''$) are shown inset in Figs. 1 and 2 for select positions in each region. We only present spectra for regions where complex or interesting line profiles were observed.

Finally, a comparison between these new [FeII] data and the H_2 observations discussed in Paper I is made in Sect. 7 and Figs. 6 and 7. First, however, we describe the [FeII] results pertaining to each source separately.

4. [FeII] spectroscopy of Class I sources

4.1. SVS 13 (HH 7-11)

The HH 7-11 outflow in NGC 1333 ($d\sim 220$ pc) has been observed extensively at near-IR wavelengths (e.g. Garden et al. 1990; Stapelfeldt et al. 1991; Carr 1993; Gredel 1996; Chrysostomou et al. 2000; Khanzadyan et al. 2002). The HH objects themselves reside along the edges of a southeastern, blue-shifted cavity that is bounded by a fast-moving molecular shell (Bachiller & Cernicharo 1990; Bachiller et al. 2000). The probable source of the flow, SVS 13, is known to have undergone an outburst in recent years (Eislöffel et al. 1991) and, from Paper I, is clearly associated with complex H_2 line emission. Recently, SVS 13 was found to be a close-binary (separation $\sim 0.3''$), with an orbital period of $\sim$1700 yrs (Anglada et al. 2000).

In Fig. 1a we show a $P-V$ plot of the region near the source. [FeII] line emission was not detected from the HH objects that were covered by the spectrograph slit (the slit extended 44$''$ to the SE, and 42$''$ to the NW; it did not reach HH 7). However, [FeII] was detected towards SVS 13. An extracted spectrum is shown inset in Fig. 1a. The profile is double peaked and blue-shifted with respect to the systemic LSR velocity of +8 km s^{-1} (Bachiller & Cernicharo 1990), which is marked with a dashed line in the $P-V$ diagram. The stronger of the two [FeII] components peaks at $V_{LSR}\sim -133(\pm10)$ km s^{-1}; the weaker component peaks at somewhere in the range -20 to -50 km s^{-1}. Both components appear to be quite broad; the *FWHM* of the stronger, higher-velocity component (HVC) measures 73($\pm$10) km s^{-1}; deeper spectra are needed to establish the width of the weaker, marginally-detected, low-velocity component (LVC), although a two-component Gaussian fit to our data suggests a similar *FWHM*.

In Fig. 3a we show a continuum-subtracted $P-V$ diagram which shows the FEL region more clearly. By employing the same spectro-astrometric technique used in Paper I (and described above) we measure the position of the brighter [FeII] HVC with respect to the source continuum position (Fig. 4). We find that the HVC is coincident with the source, to within a conservative measurement error of $\sim 0.5''$, or $\sim$110 AU. Likewise, the H_2 emission towards SVS 13 was found to be offset by less than $\sim 0.4''$ from the source (see Paper I).

4.2. B5-IRS 1 (HH 366)

The embedded YSO B5-IRS 1 ($d\sim 350$ pc) drives an extensive east-west molecular outflow (Yu et al. 1999) that excites two distant groups of HH objects, HH 366E and 366W. Much of the emission from HH 366 is situated well beyond the range of our spectrograph slit (Bally et al. 1996). There is, however, H_2 emission within 30$''$ of the source in both lobes (Yu et al. 1999). The optical knot HH 366 E5 in the eastern, blue-shifted flow lobe lies along our spectrograph slit. Although high velocity

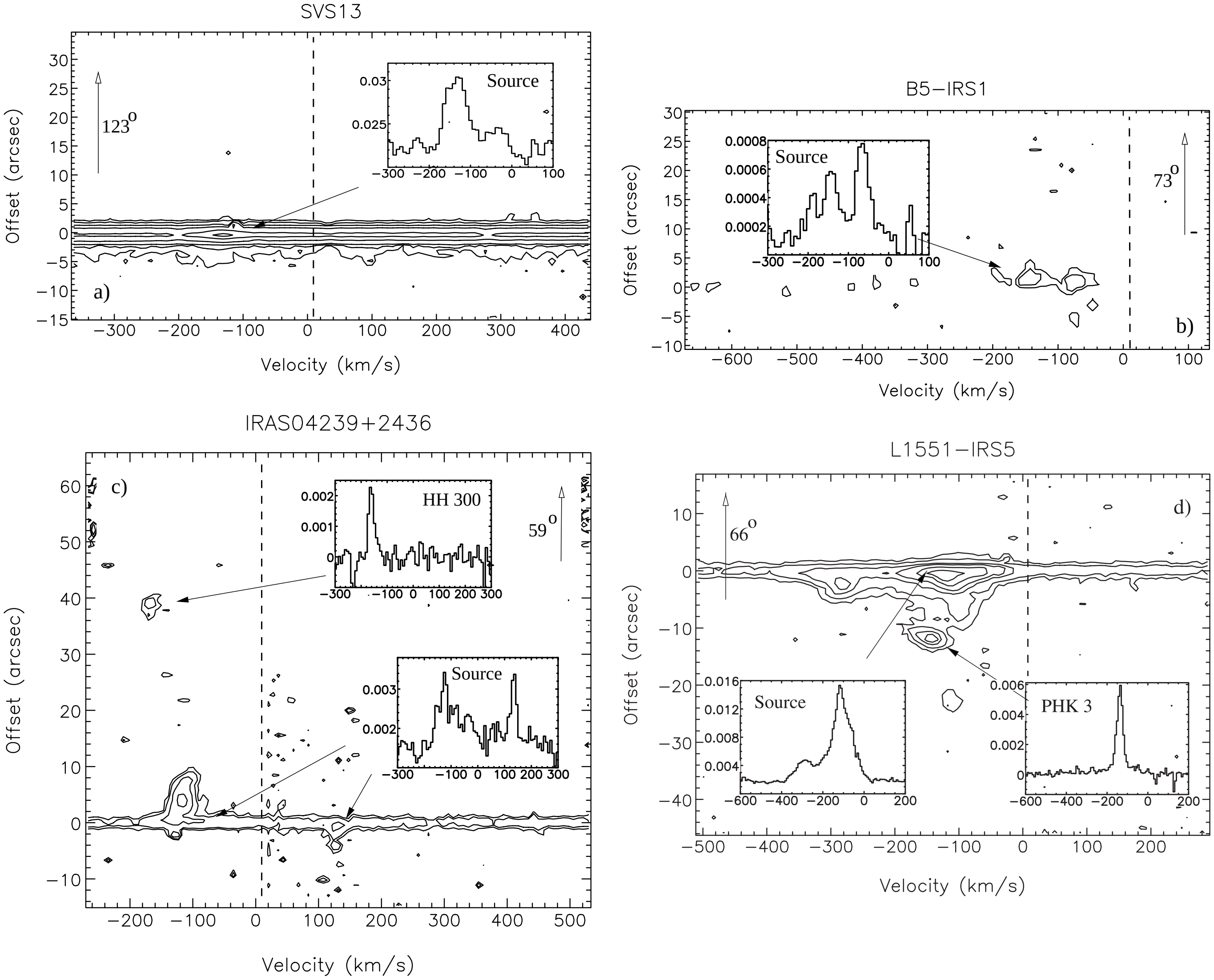

Fig. 1. [FeII] 1.644 μm *PV* plots for the Class I YSOs. *Y*-axis offsets (centred on the outflow source position) are in arcseconds along the slit. Vertical dashed lines mark the systemic LSR velocity in each region. Arrows show the slit orientation on the sky. In SVS 13 the contours measure 5, 10, 20, 50, 100 and 150× the standard deviation to the mean background, σ; in B5-IRS1 the contours are 2 and 4σ; in IRAS 04239+2348 they are 3, 5, 10 and 20σ and in L 1551-IRS5 they measure 5, 10, 20, 30, 50 and 75σ. Extracted spectra (the sum of three rows in all cases) are superimposed; the axes on all spectra are in units of km s^{-1} and Jy. Spectra are offset (from each source) by 0″ in SVS 13, 0″ in B5-IRS1, 0″ and 38.7″ in IRAS 04239+2348, and 0″ and −11.4″ in L 1551-IRS5.

H_2 emission was detected from this object (Paper I), we did not detect it in [FeII].

H_2 and [FeII] emission are detected from the source position, though in both cases the emission is very weak (see Sect. 7 for a comparison). Overall, the [FeII] emission appears to be blue-shifted (with respect to the systemic velocity of ∼10 km s^{-1}; Yu et al. 1999) to LSR velocities over a broad range from ∼−50 km s^{-1} to ∼−200 km s^{-1}.

4.3. IRAS 04239+2436 (HH 300)

The low-luminosity Class I YSO IRAS 04239+2436 in Taurus (d ∼ 140 pc) drives a highly-collimated, knotty, ∼10″-long [FeII] jet that has recently been observed in detail with NICMOS on HST (Reipurth et al. 2000). However, in these imaging data, within 1″ of the source the [FeII] jet is obscured by the continuum emission from the star. The jet also probably drives a group of extensive optical HH bow shocks (HH 300 A-C; Reipurth et al. 1997) found about 30′ to the southwest, as well as a more compact conical HH feature, HH 300 D, about 40″ to the northeast of the source.

The source itself, which is a binary (separation ∼0.3″; Reipurth et al. 2000), is notable for having a rich near-IR spectrum (Green & Lada 1996). We detect both H_2 (Paper I) and [FeII] emission from the source continuum position (see Sect. 7). In the extracted [FeII] spectrum in Fig. 1c emission from both lobes of the flow is detected. The two jet lobes must therefore be traced to within an arcsecond of the star. Moreover, extinction does little to impede our detection of the jet and counterjet in [FeII] near the source. This suggests that the flow axis must be orientated close to the plane of the sky, and that the

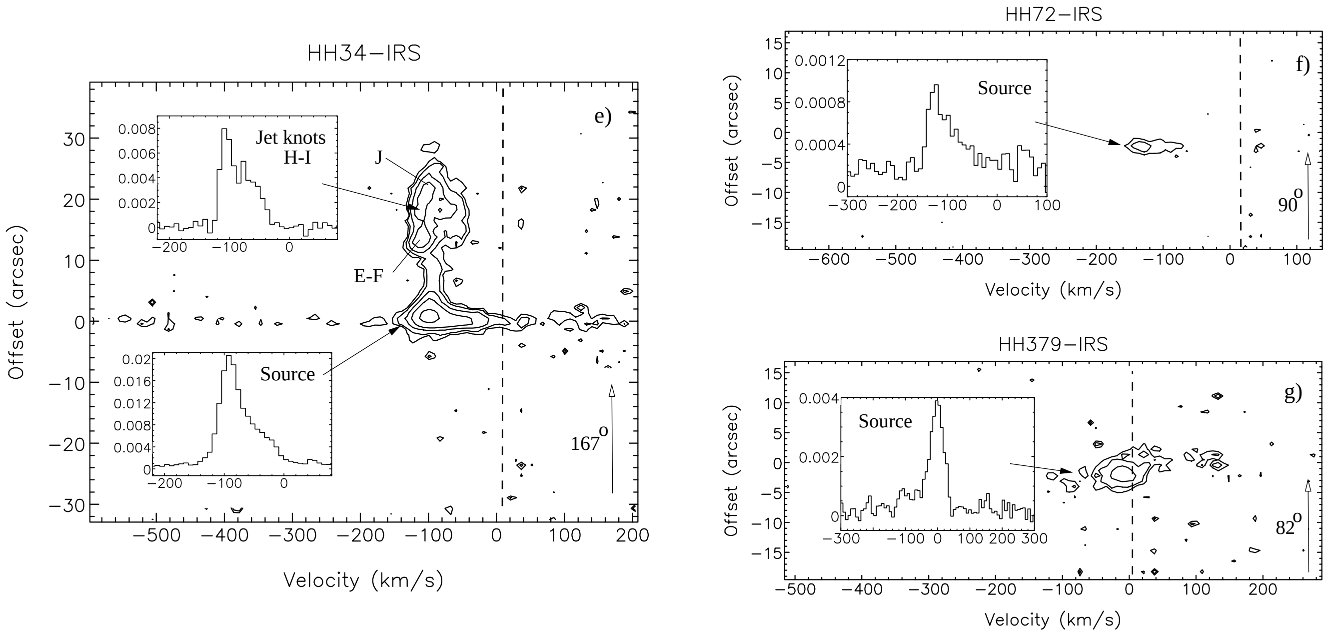

Fig. 1. Continued. In HH 34-IRS and HH 72-IRS the contours measure 3, 5, 10, 20 and 50× the standard deviation to the mean background, σ, while in HH 379-IRS they measure 5, 10 and 20σ. Spectra are offset by 0″ and 16.7″ in HH 34-IRS, 0″ in HH 72-IRS, and 0″ in HH 379-IRS.

accreting, circumstellar disk must have a thickness that is less than our 3-pixel-wide extracted region (∼2.7″, or <380 AU).

The blue- and red-shifted [FeII] line-emission components in Fig. 1c are shifted to about the same radial absolute velocity with respect to the systemic rest velocity (∼8 km s^{-1}); the peaks occur at LSR velocities of −125(±5) km s^{-1} and +133(±5) km s^{-1} respectively. The blue peak is also probably associated with a weaker, though much broader velocity component that extends from $V_{\rm LSR}$ ∼ 0 km s^{-1} to ∼−200(±10) km s^{-1}. The red counterjet peak is, on the other hand, extremely narrow (we measure a *FWHM* of 24(±3) km s^{-1}); this line is only marginally broader than the instrumental profile.

For the [FeII] observations we used a revised slit PA of 59° (an angle of 45° was used for the H_2 spectroscopy in Paper I), which is better aligned with the jet axis. In [FeII] we trace the entire ∼10″ -long blue-shifted jet lobe, as well as spatially-extended red-shifted emission from the counter-jet. These jet components are most clearly seen in the continuum-subtracted $P-V$ plot in Fig. 3b. The [FeII] line emission is strongest at an offset of 4″ (±0.5″) along the northeastern, blue-shifted jet lobe. This emission peak probably corresponds to the bright [FeII] knots J3–J5 in the HST images of Reipurth et al. (2000). In Fig. 4 we again plot the positions of these emission *peaks* with respect to the source continuum position. The 2″–5″ offsets in the blue lobe reflect the fact that the apparent [FeII] intensity increases with distance from the source. Extinction near the source is probably not the cause of this increase, since the red-shifted counterjet emission peaks closer to the source in Fig. 4b, at offsets of only ∼1″. Instead, the [FeII] emission must be enhanced along the jet axis, probably in discrete HH-type shocks. We also note in Fig. 4b that the higher-velocity blue-shifted [FeII] emission appears closer to the source. In other words, we see an apparent decrease in offset with velocity.

Finally, in addition to [FeII] emission from the source and inner jet (FEL) region, we also detect [FeII] at a distance of about 38″ to the northeast of the source. This emission is presumably associated with HH 300D (Reipurth et al. 1997). The [FeII] peak shown in Fig. 1c is blueshifted to an LSR velocity of −167(±5) km s^{-1}, though the emission line is also extremely narrow (*FWHM* = 25(±3) km s^{-1}); this suggests that the [FeII] is associated with high-velocity jet material, though with a relatively low-velocity shock within the flow.

4.4. L 1551-IRS5

L 1551-IRS5 is an archetypal bipolar molecular outflow that can be observed at relatively high spatial resolution because of its close proximity to the earth (d ∼ 140 pc). The flow consists of a striking blue-shifted, wind-swept cavity that extends over 10′ (0.5 pc) to the southwest of IRS 5 (Stocke et al. 1988; Moriarty-Schieven & Snell 1988). The cavity is associated with an array of optical and near-IR shock features (e.g. Mundt & Fried 1983; Davis et al. 1995). The source itself (which is a binary system) *appears* to drive two small-scale jets (Fridlund & Liseau 1998; Hartigan et al. 2000; Itoh et al. 2000; Davis et al. 2002). However, these jet-like features may instead represent the edges of a single collimated flow (Mundt et al. 1991; Pyo et al. 2002). Indeed, the new images of Pyo et al. represent perhaps the strongest evidence yet that the two “jets” are simply the limb-brightened edges of a small, ovoidal cavity, that is bounded at its leading edge by a bright bow, which they label PHK 3.

In H_2 we detected complex velocity structure along the L 1551-IRS5 jet (Paper I). Likewise, in [FeII], multi-component profiles are again observed, though in detail the H_2 and [FeII] emissions are very different. As we shall discuss further in Sect. 7, the LVC observed in H_2 is not detected in

[FeII]; in the latter, only an HVC and what we shall refer to as an "extremely-high-velocity component" (EHVC) is observed. The HVC and EHVC in Fig. 1d peak at $-120(\pm5)$ km s^{-1} and $-285(\pm15)$ km s^{-1} respectively (both are strongly blueshifted with respect to the systemic velocity of 6 km s^{-1}; Moriarty-Schieven & Snell 1988). Both components are also quite broad; a two-component Gaussian fit yields *FWHM* widths of $113(\pm5)$ km s^{-1} and $125(\pm15)$ km s^{-1} for the HVC and EHVC. The overall *FWZI* range in radial velocities observed in [FeII] is also roughly equal to those seen in [SII] (Hartigan et al. 2000).

In Figs. 3 and 4 we again show a continuum-subtracted $P-V$ diagram and a plot of the positions of the line-emisson peaks with respect to the source continuum. Spatially, the HVC peak is closer to the source continuum position than the EHVC; the EHVC is offset by about 2″–3″ to the southwest, about twice as far as the HVC along the blue-shifted flow axis. However, although the EHVC *peak* is offset further downwind, overall the HVC *emission* extends almost twice as far along the flow. We also note once again an apparent decrease in offset with velocity in Fig. 4c, when considering the EHVC separately. Very similar results were recently reported by Pyo et al. (2002).

Further downwind, we detect compact [FeII] peaks at offsets of ~12″ and ~23″. In velocity space both peaks are narrow; for the brighter feature we measure a *FWHM* of $40(\pm3)$ km s^{-1}. This bright peak is blue-shifted to an intermediate velocity of $-140(\pm10)$ km s^{-1}. Both features correspond to discrete knots along the jet axis. The feature at 12″ coincides with the optical/[FeII] bow shock PHK 3 (labeled knot D by Fridlund & Liseau 1998).

4.5. HH 34-IRS

The HH 34 outflow in L 1641 ($d \sim 450$ pc) is part of a parsec-scale "superjet" that includes HH 33, 40 and 85 to the north, and HH 86-88 to the south (Devine et al. 1997a). The collimated, knotty, HH 34 jet itself has been the subject of intense scrutiny at optical and near-IR wavelengths. Within 22″ of the IRS source, the jet remains highly collimated, the optical emission being confined to within a width of less than 1″ (Ray et al. 1996; Reipurth et al. 2000). The flow is orientated at an angle of ~23° to the plane of the sky, and in optical emission lines radial and tangential jet-knot velocities of ~−100 km s^{-1} and 150–300 km s^{-1} have been recorded (Bührke et al. 1988; Heathcote & Reipurth 1992; Eislöffel & Mundt 1992).

Like L 1551-IRS5, the HH 34 jet near the source is observed in both H_2 and [FeII] emission (the latter was first detected in the images of Stapelfeldt et al. 1991), though there are again differences in the details (discussed in Sect. 7). The [FeII] flux distribution closely follows that seen in [SII] (Ray et al. 1996), being much weaker within the first 10″ of the source. The [FeII] profiles along the jet, at offsets between 10″ and 20″, comprise a blue-shifted peak at $V_{\rm LSR} \sim -120$ km s^{-1} plus an extended red-wing. These broad lines appear almost double-peaked between knots E and I (Fig. 1e), although the [FeII] profiles furthest from the source (towards knot J) converge to a single, slightly less blue-shifted radial velocity of about -100 km s^{-1}. The [FeII] profiles are very similar to those seen in [SII], in terms of the velocity at the emission peak, the overall range of radial velocities observed, and the general "inverted-V" shape of the emission profile in the $P-V$ plot between knots E and J (Bührke et al. 1988; Heathcote & Reipurth 1992).

Towards the continuum source position the [FeII] profile comprises a sharp peak at $-95(\pm10)$ km s^{-1} and a broad red wing that extends back almost to the systemic rest velocity of ~8 km s^{-1} (Chernin & Masson 1995). The bulk of the [FeII] emission towards HH 34-IRS is therefore blue-shifted to velocities that are almost as high as those seen along the jet.

In Paper I we found that the H_2 emission towards HH 34-IRS is coincident with the source continuum position (unlike the other YSOs observed, where the H_2 towards the source is usually offset along the blue-shifted flow lobe by at least a few tenths on an arcsecond). Unfortunately, we detected only very weak continuum emission from HH 34-IRS in our *H*-band observations, so we cannot measure (or set accurate upper limits on) the offset between the [FeII] line emission and the continuum position.

4.6. HH 72-IRS

The distant, intermediate-mass YSO HH 72-IRS ($d \sim 1500$ pc) in L 1660 drives an east-west bipolar molecular outflow (Schwartz et al. 1988; Reipurth & Graham 1988). No collimated HH jet is observed from this YSO; optical HH emission knots are only observed near the eastern end of the flow, where it exits the dense core that harbours the powering source. However, additional shock features are detected closer to the source in H_2 emission (Davis et al. 1997, 2002). From the partial overlap between the CO flow lobes, this outflow is probably orientated at 30°–60° to the plane of the sky.

Unpublished [FeII] images obtained by one of us (CJD) reveal emission only from the optical HH 72 bow shock (the knots labelled A, B and C by Reipurth & Graham 1988). Our spectrograph slit, which was aligned along the small-scale H_2 jet axis that extends a few arcseconds to the east of the IRS source (Davis et al. 2002), passed just to the north of these [FeII] features, so they do not appear in the $P-V$ plot in Fig. 1f. However, [FeII] emission was detected towards the source continuum position. The [FeII] profile in Fig. 1f is very similar to the profile seen towards HH 34-IRS, even though it is much weaker and is associated with a more distant and more massive YSO. The [FeII] emission from HH 72-IRS peaks at $V_{\rm LSR} \sim -130(\pm15)$ km s^{-1}, while a broad red wing extends to near-zero radial velocities (with respect to the systemic rest velocity of +20 km s^{-1}; Schwartz et al. 1988).

As with HH 34-IRS, we are not able to accurately measure the offset between the line emission and the source continuum because the latter is too weak in the *H*-band.

4.7. HH 379-IRS

The HH 379 outflow is situated near the molecular cloud 093.5–04.3 in Cygnus (Dobashi et al. 1994) at a distance of

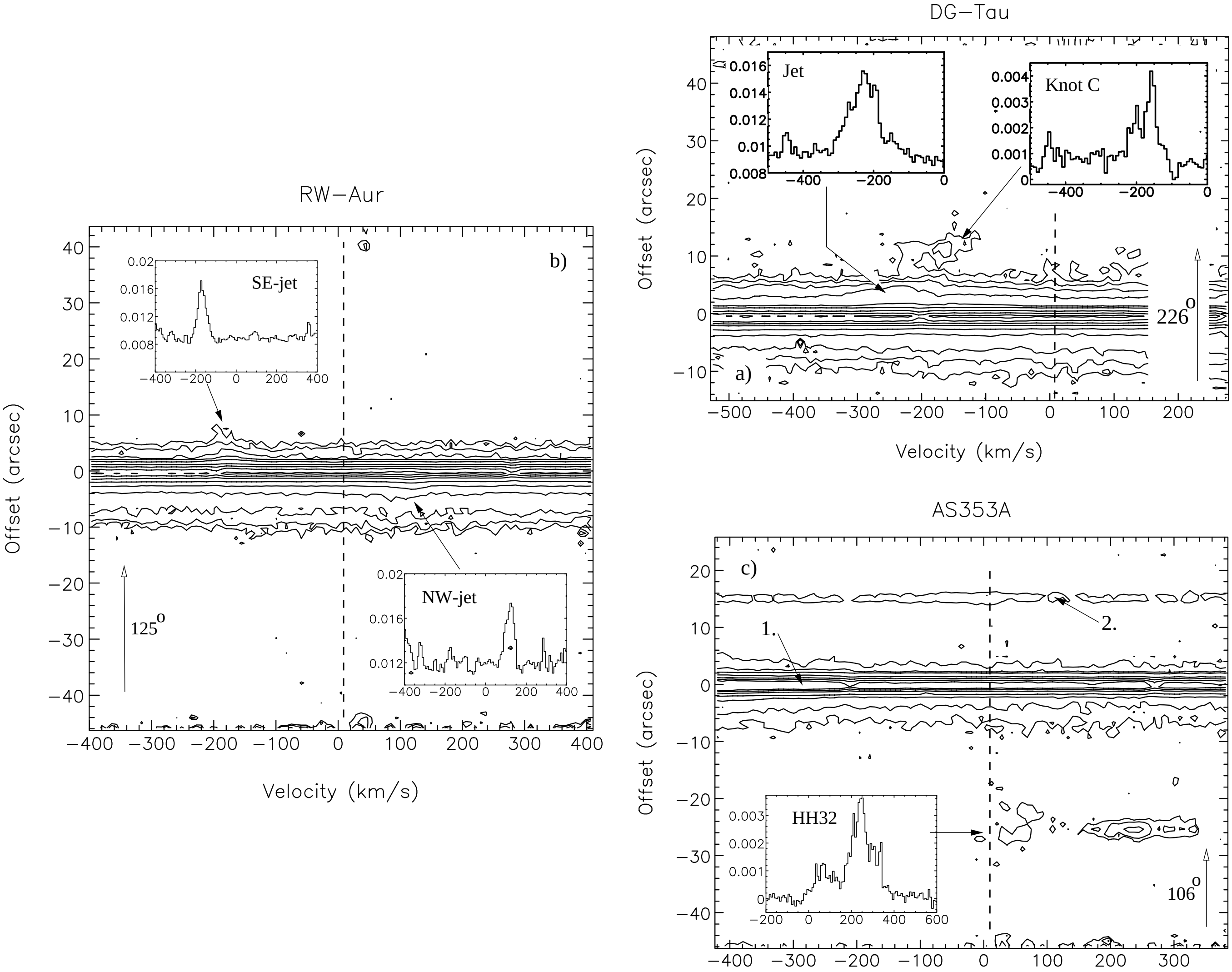

Fig. 2. Same as Fig. 1, except that in AS 353A the contours measure 5, 10, 20, 50, 100, 150, 200, 400, 800σ, while in DG Tau and RW Aur the contours represent 3, 5, 10, 20, 50... (etc.) σ. Spectra are offset by 3.5″ and 11.4″ in DG Tau, 2.6″ and −2.6″ in RW Aur, and −24.6″ in AS 353A.

~0.9 kpc. HH 379-IRS may be associated with a nearby compact optical nebula (Devine et al. 1997b). In Paper I we assumed that this conical nebula harbours the HH energy source and therefore positioned our spectrograph slit through the nebula and the HH object; we have done the same here with our [FeII] observations.

No continuum emission was detected from the outflow source in the [FeII] data. However, a distinct [FeII] line-emission peak is observed towards the nominal source position (Fig. 1g). The emission from HH 379-IRS is morphologically and kinematically very similar in [FeII] and H_2. Both H_2 and [FeII] peaks in the $P-V$ diagrams appear to be elongated at a position angle that implies a blue-shifted flow towards the west of the source and a red-shifted flow to the east. However, note that HH 379-IRS is somewhat unique amongst the Class I YSOs observed here, since it is the only source with [FeII] that peaks near the systemic rest velocity (discussed further in Sect. 7).

Again, we do not measure the offset between the line emission and the IRS source position because of the lack of continuum emission at these shorter wavelengths.

5. [FeII] spectroscopy of classical T Tauri stars

DG Tau and RW Aur were not part of our original H_2 survey (Paper I), although AS 353A was observed in the earlier study. We discuss these three sources separately below.

5.1. DG Tau (HH 158)

The classical T Tauri star DG Tau ($d \sim 140$ pc) drives a well-collimated HH jet (HH 158) that extends over about 10″ to the southwest (Mundt et al. 1987; Lavalley et al. 1997; Eislöffel & Mundt 1997). The jet itself has recently been observed at high spatial resolution, with HST by Bacciotti et al. (2000, 2002) and with adaptive optics (AO) by Dougados et al. (2000).

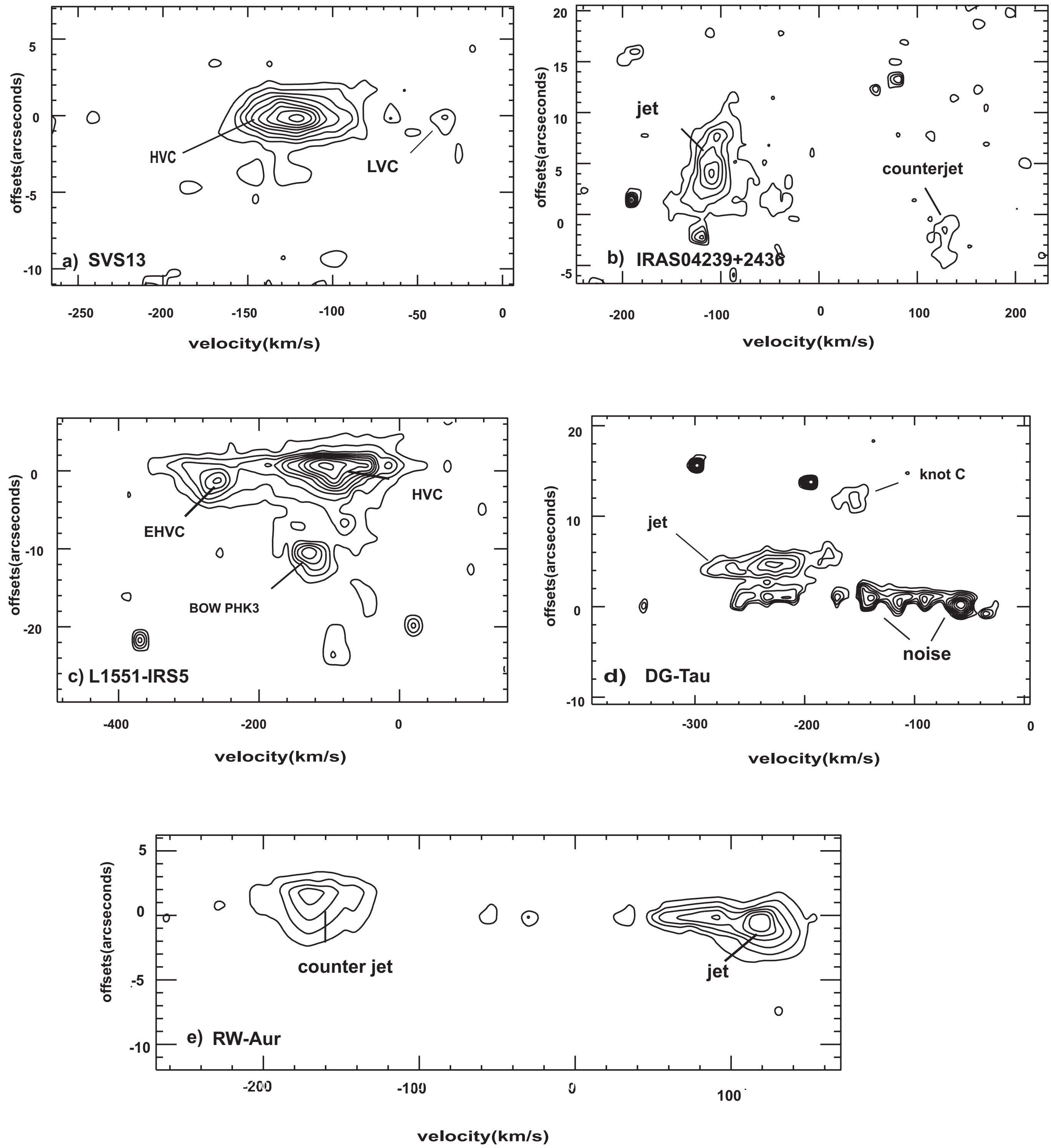

Fig. 3. [FeII] $P-V$ diagrams of five of the outflows. Only emission within approximately 15″ of each YSO is plotted. The continuum emission from each source has been fitted and removed. Contours start at the 3σ background (blank sky) noise level and increase by a factor of $\sqrt{2}$.

These data show the jet structure within a few arcseconds of the source, and even point to possible precession and/or jet-rotation on arcsecond scales. Here we adopt the same slit PA as was used by Bacciotti et al. (1998) in their HST STIS observations.

Hamann et al. (1994) report the detection of blue-shifted [FeII] 1.644 μm emission from DG Tau, though they did not observe along the jet axis. Takami et al. (2002) show [FeII] 1.257 μm spectra which likewise exhibit high, blue-shifted velocities, though again their spectrograph slit was not aligned with the jet axis. Here we detect [FeII] *predominantly from* the DG Tau jet (although we do not detect a counter-jet). In these data, within 1″–2″ of the source the [FeII] peaks at $V_{\rm LSR} = -235(\pm10)$ km s^{-1} (this spectrum is labelled "jet" in Fig. 2a) while further downwind (offset −11.4″), towards

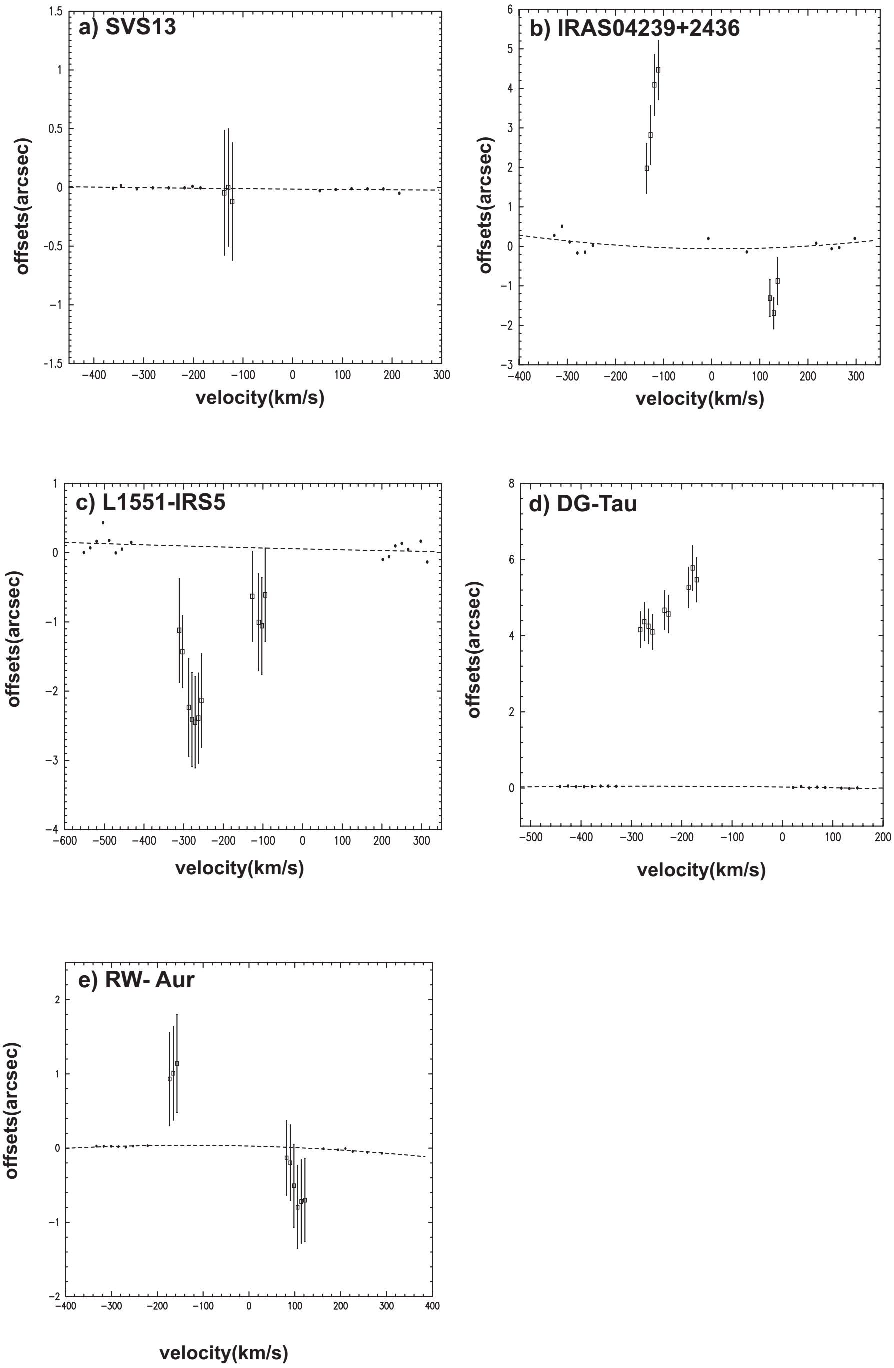

Fig. 4. Offsets of the [FeII] emission peaks from the stellar continuum centroid. The boxes (with error bars) represent the [FeII] positions, measured in each column (at each velocity bin) from the $P-V$ diagrams. The points at high (blue- and red-shifted) velocities are measures of the continuum position. The dashed line in each plot is a polynomial fit to these continuum points; these lines show the source continuum position.

the bow-shock-like knot labelled knot C by Eislöffel & Mundt (1997), the [FeII] peaks at $V_{\rm LSR} = -150(\pm10)$ km s^{-1}. Note that for DG Tau the systemic LSR velocity is 6.0 km s^{-1} (Kitamura et al. 1996) and that the weak features at -460 km s^{-1} in the two spectra in Fig. 2a represent the same artefact, namely an imperfectly-subtracted sky line.

The decrease in velocity between the source and bow shock C in the DG Tau jet is continuous along the weaker [FeII] emission observed between these two features. The [FeII] is broad near the source ($FWHM \sim 100(\pm5)$ km s^{-1}) though the profile narrows further downwind. The [FeII] radial velocities compare very closely with published [SII] observations (Mundt et al. 1987; Bacciotti et al. 2000).

In Fig. 3d we show a continuum-subtracted $P-V$ diagram which more clearly shows the [FeII] emission near DG Tau. In Fig. 4d we plot the positions of these [FeII] emission peaks with respect to the source continuum. As with some of the Class I sources, we see that the offset of the FEL emission decreases with increasing blue-shifted velocity.

High-resolution optical observations of the DG Tau jet, in [SII] and [NII], reveal a compact knot at a projected distance of about $0.6''$–$0.8''$ from the source and a broader bow shock feature at a distance of $3''$–$4''$ (labelled A1 by Bacciotti et al. 2000). Based on the offsets recorded in Fig. 4d we associate the [FeII] emission with this bow shock. Excitation in a bow shock would certainly explain the broad emission-line profile shown in Fig. 2a. The *FWZI* of the profile points to a high shock velocity, of the order of 200 km s^{-1}. If this bow shock is an "internal working surface", associated with faster jet material catching up with slower jet gas, then the velocity difference between these two outflow episodes must be very high.

Within 1″ of DG Tau we do not detect any [FeII] emission. The knots in Fig. 3d (labelled "noise") are due to Shot noise associated with the bright source continuum emission; further along the slit, where the data are read-noise limited, noise levels are lower so faint [FeII] emission can be detected. Thus, any similarly weak [FeII] associated with the [SII] knot observed within 1″ of the source (knot A2; Bacciotti et al. 2000) could easily be lost in this noise.

5.2. RW Aur (HH 229)

RW Aur is a complex multiple star system located in Taurus-Aurigae (d ~ 140 pc). The HH 229 jet is associated with the brightest stellar component "A", a classical T Tauri star which may itself be a spectroscopic binary (Gahm et al. 1999). The fainter components "B" and "C" form a close binary system (separation 0.12″) that is situated about 1.5″ away. The lobes of the bipolar jet from RW Aur-A (hereafter referred to as simply RW Aur) are visible over a considerable distance; Mundt & Eislöffel (1998) report a jet length of ~145″. In optical forbidden lines, radial velocities of 100–200 km s^{-1} have been observed along the central 20″ of the jet (Hirth et al. 1994; Bacciotti et al. 1996). Recently, this region of the jet has been observed at high spatial resolution, using AO imaging (Dougados et al. 2000) and HST STIS spectroscopy (Woitas et al. 2002). Woitas et al. estimate an inclination angle for the jet of <37° to the plane of the sky.

In [FeII] we detect emission from both lobes of the bipolar jet (Figs. 2b and 3e). Again, the emission peaks are offset along the jet axis, by 0.5″–1.0″ with respect to the source continuum centroid (Fig. 4e), with the red-shifted [FeII] emission peaking closest to the source. AO and HST STIS observations of RW Aur show that, in the optical, both lobes of the jet are knotty, though well collimated (*FWHM* < 0.6″; Dougados et al. 2000; Woitas et al. 2002). Woitas et al. find that the [SII] flux along the blue-shifted jet lobe is rather evenly distributed within ~2″ of RW Aur; in [FeII] the emission is also extended over this same region (Fig. 3e). In the red-shifted counterjet, however, the flow appears more knotty on subarcsecond scales in the [SII] data. We do not have the spatial resolution to resolve these knots in [FeII], though we do see emission along the length of this [SII] counterjet. We also note that, as in [SII], the red jet lobe is more extended at higher velocities (between $V_{\rm LSR}$ ~ 100 km s^{-1} and 160 km s^{-1}) than it is at lower velocities ($V_{\rm LSR}$ ~ 50–100 km s^{-1}; see Fig. 3e). Moreover, in Fig. 4e there is some evidence that the [FeII] *peak* is slightly further offset at higher (red-shifted) velocities.

From the [FeII] profiles in Fig. 2b we measure peak radial LSR velocities of −175(±10) km s^{-1} and +150(±10) km s^{-1} for the jet and counterjet features (the systemic LSR velocity is ~6 km s^{-1}; Ungerechts & Thaddeus 1987). On similar spatial scales, Hirth et al. (1994) measure [SII] radial velocities for the southeastern jet and northwestern counterjet of −190 km s^{-1} and +100 km s^{-1} respectively (note that we use the same slit PA). The [FeII] line profiles in Fig. 2b are narrow, however: Gaussian fits yield line widths at *FWHM* of ~50 km s^{-1} for both lobes in RW Aur. We do not detect *any* [FeII] emission at low radial velocities, in either jet lobe (the [SII] emission is weaker, though still observed, at these low radial velocities). In other words, no LVC is detected in [FeII] in either lobe. This current lack of an LVC in FEL emission was also noted by Woitas et al. (2002) in their optical [SII] and [OI] observations. These authors have suggested that the LVC may well be variable on a timescale of a few years.

The highly blue- and red-shifted radial velocities evident in the [FeII] spectra indicate that the emission must be associated with fast-moving gas along the RW Aur flow axis. However, as with some of the other sources discussed above, the narrow line widths point to low shock velocities. Higher shock velocities are predicted for DG Tau (discussed above), where the [FeII] profiles are much wider (note that in HST images the bow shock feature A1 in DG Tau is laterally more extended than the knots in DG Tau; i.e. it has more extended wings).

5.3. AS 353A (HH 32)

The classical T Tauri star AS 353A (d ~ 300 pc, Mundt et al. 1983; Eislöffel et al. 1990) drives an obliquely-viewed bipolar HH flow, known as HH 32 (Hartigan et al. 1986; Davis et al. 1996; Curiel et al. 1997). Optical and near-IR images and spectroscopy of the leading, redshifted HH 32 bow shock are convincingly modelled if the flow is inclined at an angle of ~60° to the plane of the sky (Solf et al. 1986; Hartigan et al. 1987; Davis et al. 1996).

As was the case in Paper I, two stars were detected along the single slit position observed in the AS 353A region, which we again label 1 and 2 in Fig. 2c (AS 353A itself, the apparent source of the bipolar HH 32 outflow, is referred to as star 1; note, however, that star 2 is not AS 353B). H_2 emission was detected from star 2, and not from star 1; we did not detect [FeII] from either.

We do detect spatially-compact [FeII] from the leading edge of the HH 32 bow shock. As expected, the [FeII] profile is red-shifted to very high radial velocities; the double-peaked profile in Fig. 2c comprises components at +70(±20) km s^{-1} and +235(±10) km s^{-1} while, overall, the emission extends over *FWZI* ~ 400 km s^{-1}(the systemic LSR rest velocity is at ~8 km s^{-1}; Edwards & Snell 1982). The [FeII] profile is again quite similar to its optical counterpart in [SII], where double-peaked lines with components at ~+60 km s^{-1} and +270(±10) km s^{-1} have been reported (Hartigan et al. 1987). However, in the [SII] spectra discussed by Hartigan et al. the low-velocity component is much stronger than the high-velocity peak; in our [FeII] data, we see the opposite behaviour. This is because the optical profile is summed across the whole HH 32 clumpy bow shock region, while our single slit passes through only the centre of the bow (it largely bypasses the limb-brightened bow shock wings, seen clearly and labelled knots B and C in high-resolution optical images; e.g. Curiel et al. 1997).

Observing more of the emission from the bow wings would certainly explain the "enhanced" lower-velocity component in the [SII] profile. The double-peaked [FeII] profile in Fig. 2c, and the low-velocity H_2 reported in Paper I, do therefore comply with previously published bow shock model fits to kinematic studies of HH 32 (e.g. Hartigan et al. 1987; Davis et al. 1996).

6. Br12 observations

The Br12 HI recombination line ($\lambda_{\rm vac}$ =1.641168 μm) was included within the wavelength coverage of our echelle observations. The difference between the Br12 and [FeII] rest wavelengths is -0.00283 μm, which is equivalent to a velocity shift of 516 km s^{-1}. Br12 was detected in two Class I sources and in all three T Tauri stars. These data are presented in Fig. 5, with the rest wavelength of Br12 set to $V_{\rm LSR}$ = 0 km s^{-1}.

In SVS 13 the Br12 spectrum is broad and possibly slightly asymmetric (Fig. 5a). Gaussian fitting yields a *FWHM* of $-181(\pm10)$ km s^{-1} and a peak velocity of $-2(\pm4)$ km s^{-1}, although the actual intensity peak is shifted to about -20 km s^{-1}. A similarly broad, low-velocity line is observed towards the only other Class I YSO that we detected in Br12 emission, IRAS 04239+2436 (Fig. 5b). Fits yield a *FWHM* of 239($\pm$18) km s^{-1} and a peak velocity of +3($\pm$9) km s^{-1} for this source.

Br12 emission was detected towards all three T Tauri stars (Figs. 5c–e), where the integrated line luminosities were at least 5$\times$ stronger than they were for the Class I YSOs. In DG Tau, the Br12 profile is blended with blue-shifted [FeII] emission, which in the rest frame of the HI line appears at high (>250 km s^{-1}) radial velocities (indicated in Fig. 5c). The Br12 is, nevertheless, again very broad and centred near the systemic rest velocity. The RW Aur Br12 profile in Fig. 5d is markedly asymmetric and strongly blue-shifted. The line consists of a central peak at $-95(\pm5)$ km s^{-1} and broad blue and redshifted line wings. The profile extends over about 600 km s^{-1} *FWZI*. In AS 353A we observe very strong Br12 emission. The profile towards this source is notable for being extremely symmetric and Gaussian in shape, with no sign of enhanced line-wing emission, nor blue or red-shifted absorption features. Overall, the width of the AS 353A profile (*FWHM*) measures 274($\pm$6) km s^{-1}; the line also peaks at a very low radial velocity of +16($\pm$2) km s^{-1}.

HI observations of many of our targets were also presented in Paper I, where the *K*-band Brγ emission line was observed. The same slit positions and slit angles were used for the Brγ data as were used for Br12/[FeII] and H_2. Brγ was detected towards four Class I YSOs; SVS 13, IRAS 04239+2436, HH 34-IRS and GGD 27(1), as well as towards the only T Tauri star studied in Paper I, AS 353A. Here we detected Br12 in the same Class I sources, except for HH 34-IRS and GGD27 (the latter was not observed at 1.64 μm). Our Br12 non-detection for HH 34-IRS was not unexpected since the Brγ line was very weak in this source and, for the other Class I sources, the Br12 emission was 120–160$\times$ weaker than Brγ. For AS 353A, the ratio is lower, Brγ/Br12 $\sim$ 35, because of the reduced extinction to this source. Indeed, extinction is probably the main cause of the differences in line ratios observed. For $T_{\rm e}$ $\sim$ 10^4 K and $N_{\rm e}$ $\sim$ 10^4 cm^{-3} a ratio of 5 is expected (Hummer & Storey 1987); this ratio is observed in dense shock regions and PDRs like Orion Peak-1 and Hubble 12 (Everett et al. 1995; Luhman & Rieke 1996). Assuming similar excitation conditions, the Brγ/Br12 ratio may therefore be used to roughly estimate the extinction to the HI region. The difference in extinction at 1.6 μm and 2.2 μm may be written as:

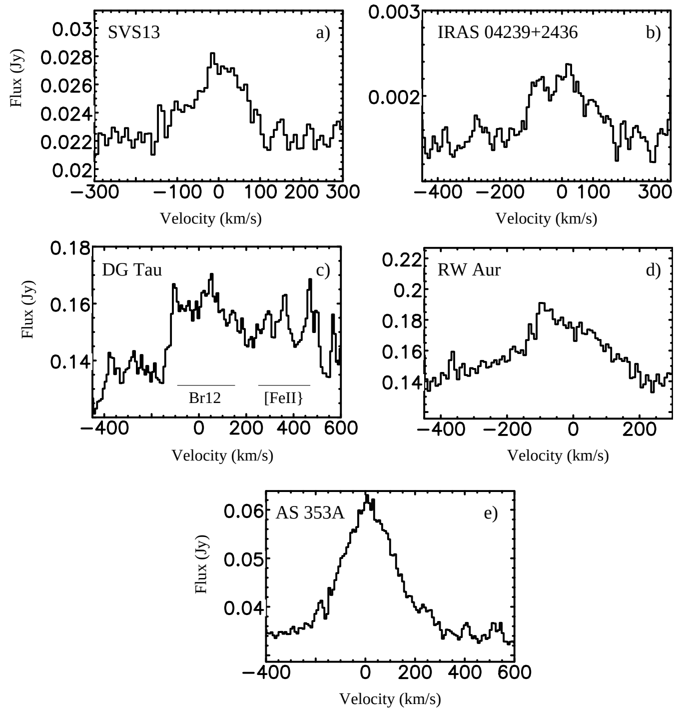

Fig. 5. Br12 spectra towards the source continuum positions in five regions (the sum of three adjacent rows is again plotted). Br12 was not detected in any of the other YSOs. Stationary [FeII] emission would be offset by +512 km s^{-1} in these spectra.

$$A_{1.6} - A_{2.2} \sim 2.5 \log(0.2 \times I_{\rm Br\gamma}/I_{\rm Br12}) \qquad (1)$$

where $I_{\rm Br\gamma}/I_{\rm Br12}$ is the ratio of integrated Brγ and Br12 line fluxes (observed here and in Paper I). If $A_{2.2}$ = 0.112 $A_{\rm v}$, and $A_{1.6}$ = 0.175 $A_{\rm v}$ (Rieke & Lebofsky 1985), then for the Class I sources where $I_{\rm Br12}/I_{\rm Br\gamma}$ $\sim$ 140 an extinction of $A_{\rm v}$ $\sim$ 60 is predicted. This is not unreasonable if the HI emission lines derive from the inner regions of the accretion disk and/or the first few AU of the jet, as we argue below.

In Paper I we identified the Brγ emission with hot gas in the inner disk and accretion flow, rather than with outflow material, because the Brγ emission was found to be spatially coincident with each source and confined to the source position (i.e. the emission was not extended along the outflow axis, unlike the H_2 and [FeII]). The Brγ profiles were also found to be very broad, typically $\geq$200 km s^{-1} *FWHM*, symmetric in shape, and slightly blue-shifted, typically by 10–30 km s^{-1}. Such profiles could be due to a combination of keplerian rotation in the inner regions of a circumstellar disk (within 0.1–0.01 AU of a 1 $M_\odot$ star) and magnetospheric accretion (Hartmann et al. 1994; Muzerrolle et al. 1998), although accretion models do tend to produce red-shifted absorption features, which were not observed in Paper I and are statistically rare in optical and near-IR surveys of HI emission from T Tauri stars (e.g. Reipurth et al. 1996; Folha & Emerson 2000). In any case, the Br12 emission in the five YSOs observed here appears to have a similar origin, since the profiles in Fig. 5 are all broad and they peak at low radial velocities. From Gaussian fits to cuts made perpendicular to the dispersion axes in our $P-V$ plots, we also find that the Br12 peaks are coincident with the stellar continuum centroids (to an accuracy of <1″), and that the emission is not extended along the slit/outflow axes.

The one possible exception to the characteristics described above is RW Aur. Here the Br12 profile is blue-shifted and clearly asymmetric. The velocity shift and the extensive blue wing evident in Fig. 5d could be explained in terms of emission from an outflow, although we do not see clear evidence in our data that the Br12 emission is extended along the jet axis. The permitted HI Brackett lines are not usually detected in outflows on large, arcsecond (>100 AU) scales. However, HI may be excited at the very base of some CTTS jets. In the optical, Takami et al. (2001) have measured spatial offsets – on AU scales – in the high-velocity wings of their Hα spectra of the CTTS RU Lupi. This suggests that the emission could, at least in part, be excited in the flow. Consequently, although the excitation conditions necessary for Brackett line emission are typically not met in the extended outflow lobes and HH objects, they may be met in a jet within a few AU of the central source. Higher-resolution, near-IR spectro-astrometric observations of embedded YSOs, similar to those acquired by Takami et al. (2002) for DG Tau, are urgently needed to study these regions in more detail.

Finally, we briefly consider why we do not detect Br12 (nor indeed Brγ in Paper I) towards all of the YSOs observed. Although extinction and, to a lesser extent, differing excitation conditions may play a role, the lack of Brγ and Br12 emission towards the majority of the Class I sources may be due to the fact that the embedded source, and therefore the line emission region, is not observed directly. If this is the case, then the continuum emission we detect in the K-band and, particularly, the H-band may be nebulosity associated with the YSO that is slightly offset from the true source position, rather than photospheric emission from the protostar. On the other hand, if HI emission *is* observed (as is the case for two of the most interesting Class I YSOs, SVS 13 and HH 34-IRS), then we may be confident that we are observing the source directly, and that the offsets reported above (and in Paper I) between the MHEL and FEL regions and the continuum centroids are indeed between the emission line regions and the central stars in each case.

7. Comparison of the [FeII] data with the H_2 observations in Paper I

Having described the [FeII] and H_2 observations in Sect. 4 above and in Paper I, we now compare the two data sets for each source in some detail. To aid with this comparison, we plot in Fig. 6 H_2 and [FeII] spectra on the same plot axes. In both cases the spectra represent the sum of three adjacent rows centred on the source continuum position, so they effectively cover the same area on each YSO. We assume that any slight spatial shift in the absolute position of the slit with respect to the source, caused by a combination of orientation and the change in extinction between the H and K-bands, is insignificant.

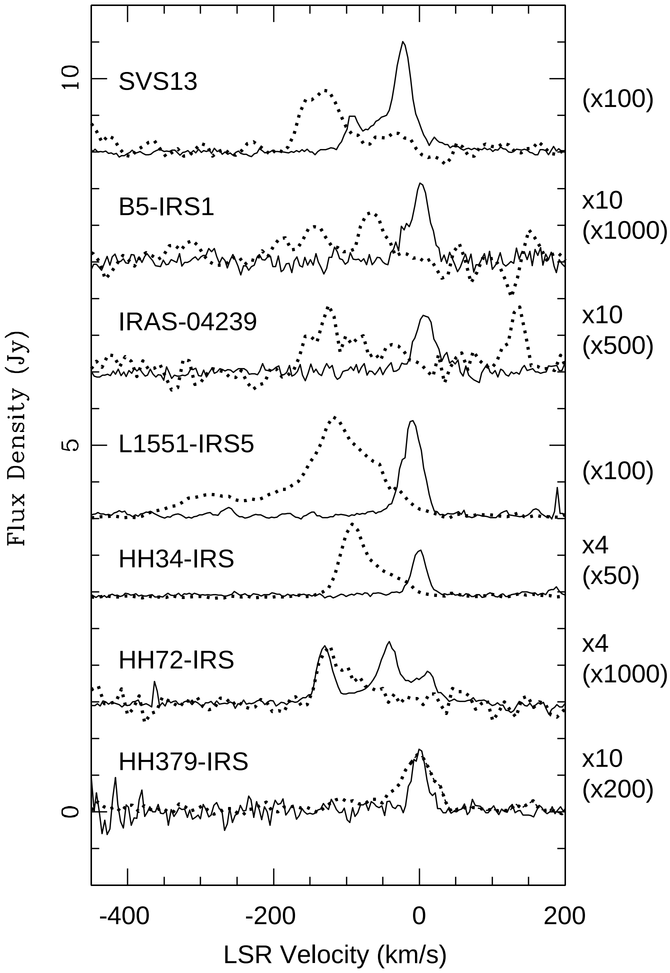

Fig. 6. A comparison of the [FeII] and H_2 spectra extracted from the source-continuum position in each target (the H_2 and [FeII] spectra represent the same 3-row-wide area on each source). H_2 spectra are drawn with full lines; [FeII] data with thick, dotted lines. The spectra have been multiplied by the values shown to the right of each plot (H_2 multiplication factor is unbracketted; [FeII] factor is bracketted). A constant has also been added to each plot so that all data can be included in the same figure.

Line peak velocities and line widths derived from the spectra in Fig. 6 are listed in Table 2. In most cases these are measured from multi-component Gaussian fits to each profile, although for B 5-IRS1, L 1551-IRS 5 and HH 34-IRS the parameters were measured "by eye" from the spectra, since these lines are clearly non-Gaussian in shape. The errors on the individual velocities are probably dominated by systematic effects (as described in Sect. 2) rather than by errors in the fitting; errors in $V_{\rm peak}$ and V_{FWHM} are therefore of the order of <10 km s^{-1}.

In L 1551-IRS5 and HH 34, where complex line emission spectra were detected along the jet axes, in both H_2 and [FeII], we also show (in Fig. 7) $P-V$ diagrams plotted side-by-side, and discuss these jets further in Sect. 7.2.

7.1. Line emission towards each outflow source

Towards SVS 13, the [FeII] and H_2 profiles in Fig. 6 are both complex and double-peaked. The H_2 components peak at lower radial LSR velocities, $-20(\pm5)$ km s^{-1} (LVC) and $-90(\pm5)$ km s^{-1} (intermediate-velocity component, or IVC), as compared to $-35(\pm15)$ km s^{-1} (LVC) and $-133(\pm10)$ km s^{-1} (HVC) in [FeII]. The most significant difference in these data is the fact that, in H_2, the intermediate-velocity component (IVC) is weaker than the LVC, while in [FeII] the opposite is the case – the HVC dominates. Also, overall the [FeII] profile is about twice as broad as the H_2 profile. It therefore seems likely that, although both low- and intermediate/high-velocity components are observed in H_2 and [FeII], the latter is nevertheless a better tracer of the highest flow velocities at the base of the jet.

H_2 and [FeII] emission profiles observed towards B5-IRS 1 are also shown in Fig. 6. The H_2 profile is mildly asymmetric, exhibiting a weak blue-shifted wing that extends out to about -40 km s^{-1}. The line profile is centred at $\sim$+4($\pm$5) km s^{-1}, close to the systemic velocity of $\sim$10 km s^{-1}, though it extends over almost 100 km s^{-1} *FWZI*. The [FeII] profile may be double-peaked, though our detection is marginal. Overall, the [FeII] emission appears to be blue-shifted with respect to the H_2.

Towards IRAS 04239+2436 only a single LVC is observed in H_2; the profile peaks within a few km s^{-1} of the systemic velocity. By comparison, [FeII] traces much higher radial velocities, in both the blue and red jet lobes (Table 2). Note, however, that for the [FeII] observations we used a different slit PA of 59° (an angle of 45° was used for the H_2 spectroscopy in Paper I), which is better aligned with the jet axis.

Towards the *H*-band continuum position of L 1551-IRS 5 a multi-component [FeII] spectrum is observed (Fig. 6); at least two components are identified, a bright HVC at ~-120 km s^{-1} and an EHVC at -285 km s^{-1}. In H_2, a single LVC is observed, peaking at approximately -7 km s^{-1}, though there is a blue-shifted "bump" at ~-25 km s^{-1} superimposed onto this, otherwise Gaussian, line profile.

Near HH 34-IRS the [FeII] is strongly blue-shifted, while the much narrower H_2 profile peaks at a relatively low velocity (Table 2). The H_2 peak velocity is considerably lower towards the source position than it is along the jet, while in [FeII] the emission towards HH 34-IRS is almost as high as it is along the jet (described further below).

The [FeII] emission from HH 72-IRS peaks at $V_{\rm LSR} \sim -130$ km s^{-1}; a broad red wing extends to near-zero radial velocities. By comparison, very complex H_2 line emission is observed towards HH 72-IRS. The H_2 profile comprises at least three velocity peaks, an LVC at +13 km s^{-1}, an IVC at -40 km s^{-1} and an HVC -130 km s^{-1}; these are superimposed on to a blue wing that extends to a velocity of ~-165 km s^{-1}. The [FeII] peak appears to be associated only with the most blue-shifted component, the HVC.

Lastly, towards HH 379-IRS, the H_2 and [FeII] profiles peak at almost the same, low, radial velocity (Table 2). This is in stark contrast to the other sources in Fig. 6; in all other sources the [FeII] towards the central YSO is strongly blue-shifted. These low H_2 and [FeII] radial velocities in HH 379-IRS could simply be due to the orientation of the flow with respect to the line of sight (which is not well known), if the flow lies in the plane of the sky. The [FeII] may still trace the higher-velocity jet component. Notably, the [FeII] line is about twice as broad as the H_2 profile, as would be expected in such a scenario (Table 2).

To summarise then, within a distance along each outflow axis of less than an arcsecond (i.e. within approximately 140 AU–1500 AU of the outflow source, depending on the distance to the target), for all Class I sources observed, the [FeII] emission is accelerated to much higher radial velocities than the H_2 emission (see also Table 2).

7.2. H_2 vs [FeII] in the L 1551-IRS 5 and HH 34 jets

Complex H_2 and [FeII] line emission is also observed along the inner jet regions in L 1551-IRS 5 and HH 34. In Fig. 7 we show these $P-V$ diagrams together for ease of comparison.

In the L 1551-IRS 5 system we detect H_2 line emission in both the blue jet and (weakly) in the red-shifted counterjet. The counterjet is not detected in [FeII], presumably because of increased extinction at these shorter wavelengths. In the south-western blue lobe (negative offsets in Fig. 7) the H_2 velocities are generally much lower than the [FeII] velocities. A bright H_2 feature is observed at an offset of $-6''$ with a radial velocity of -55 km s^{-1} which has no obvious compact [FeII] counterpart (although diffuse [FeII] is detected in this region with $V_{\rm LSR} \sim -100$ km s^{-1}), and double-peaked H_2 is observed towards knot PHK 3 (as compared to the single, narrow [FeII] component). For PHK 3, the combined [FeII] and H_2 observations can be understood in terms of a geometrical bow shock model, if the H_2 is excited in the oblique bow wings, with the [FeII] produced in the high-velocity/high-excitation bow shock cap (e.g. Hartigan et al. 1987; Tedds et al. 1999).

Along the HH 34-IRS jet axis (positive offsets in Fig. 7) the H_2 and [FeII] emission features peak at very similar blue-shifted velocities, even though the H_2 and [FeII] emissions are clearly excited in different regions of the flow. H_2 is observed just ahead of knot L and between the source and the first optically-bright HH knot in the jet (knot E), while the [FeII] is brightest between these two regions, at offsets of $10''$–$25''$. The [FeII] profiles along the jet clearly comprise a blue-shifted peak ($V_{\rm LSR} \sim -120$ km s^{-1}) plus an extended red-wing. At higher spectral resolution these profiles would probably appear double-peaked between knots E and I, though the [FeII] profiles furthest from the source (towards knot J and K) converge to a single, slightly less blue-shifted radial velocity of about -100 km s^{-1}. By comparison, the H_2 profiles along the jet are narrower, single-peaked and centred at a radial velocity of ~-90 km s^{-1}. Collectively, these [FeII] and H_2 characteristics can, once again, be understood in terms of excitation in unresolved bow shocks. We identify the [FeII] emission features with the optical knots E–K (Bührke et al. 1988; Ray et al. 1996). These features are spatially resolved in the HST images of Ray et al. (1996). The double-peaked [FeII] profile at offsets of $18''$–$20''$ probably derives from the bow-shock shaped knot I, which in [SII] is one of the broadest and brightest knots in the inner jet region. The [FeII] line widths (and indeed the

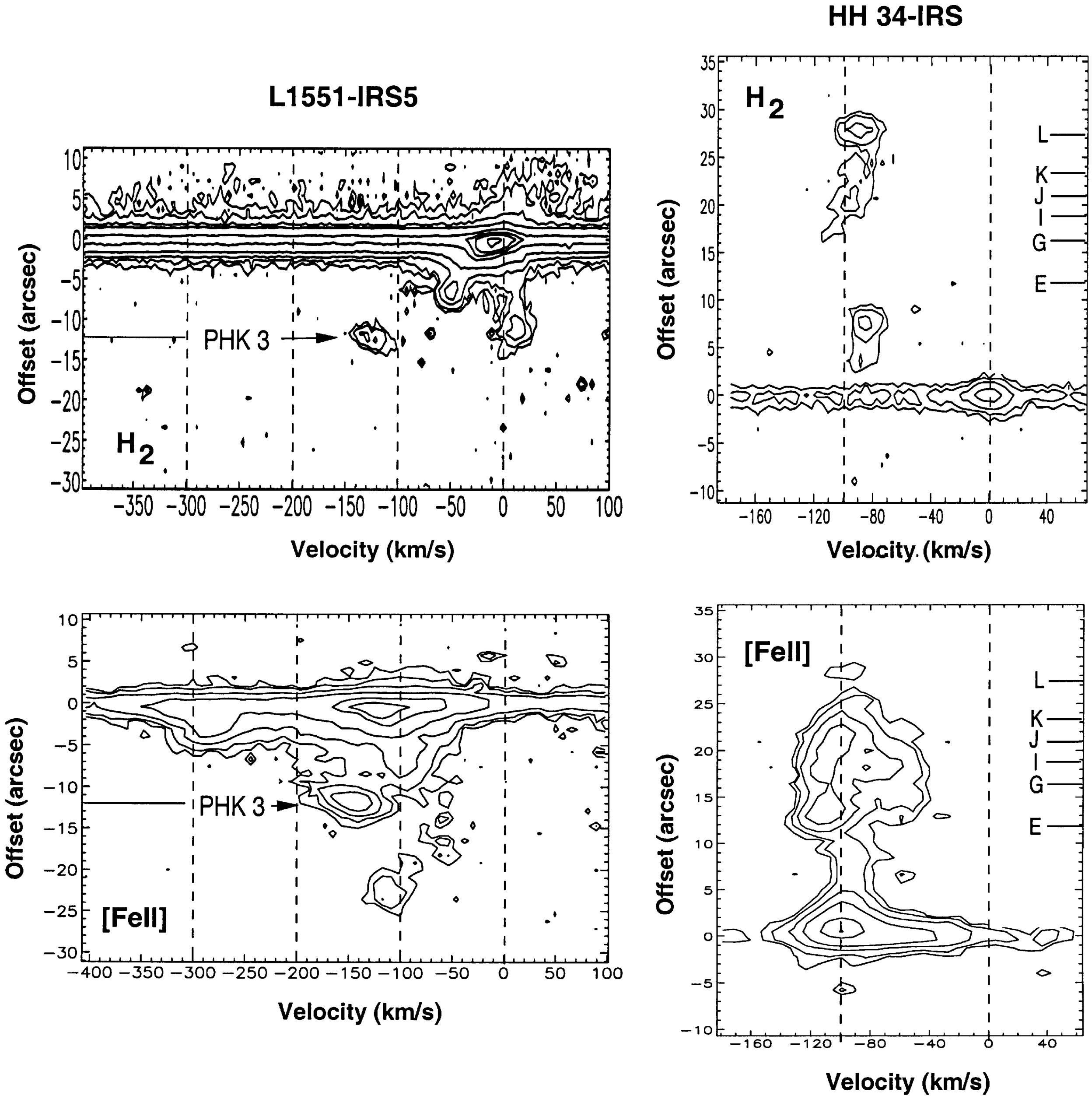

Fig. 7. A comparison of the [FeII] and H_2 $P-V$ diagrams for L 1551-IRS 5 and HH 34-IRS. In each plot the contours increase in multiples of the 1σ blank-sky noise level: 3, 5, 10, 20, 50, 75, and 100. The orientation of each $P-V$ plot on the sky is the same as in Figs. 1d and 1e. The systemic rest velocity for L 1551-IRS5 and HH 34-IRS is +6 km s^{-1} and +8 km s^{-1} respectively.

presence of [FeII] emission in the HH34 jet), suggests excitation in J-type shocks with velocities of the order of 100 km s^{-1}. Because each bow is running into fast-moving pre-shock gas, the H_2 profiles may also be strongly blue-shifted (because the gas is non-stationary) although the lines will be much narrower, since the molecular gas must be excited (rather than dissociated) in the oblique bow shock wings, where incident shock velocities will be low.

8. FELs and MHELs – Emission from the base of an outflow

The [FeII] observations reported in this paper have kinematic and spatial characteristics that are very similar to [SII] observations of jets from YSOs, in the outflows from the Class I YSOs and the CTTS jets. We may be certain, therefore, that [FeII] is a powerful tracer of FEL regions towards HH energy sources, particularly at high velocities and amongst the more deeply-embedded near-IR Class I sources.

We have compared in detail the [FeII] data with the H_2 observations from Paper I. We find that the H_2 traces a low-velocity molecular flow component (which is notably absent from the jet driven by the only T Tauri star observed in Paper I, AS 353A) while the [FeII] traces intermediate and high-velocity gas (from both Class I YSOs and CTTSs).

Towards the Class I outflow sources themselves, the [FeII] profiles are usually very wide and strongly blue-shifted, to

Table 2. Characteristics of the different velocity components seen in [FeII] and H_2.

Source/ velocity Component	[FeII] $^{1}V_{\rm peak}$ (km s^{-1})	[FeII] $^{2}\Delta V_{FWHM}$ (km s^{-1})	[FeII] $^{3}\alpha_{\rm [FeII]}$ (degrees)	H_2 $^{1}V_{\rm peak}$ (km s^{-1})	H_2 $^{2}\Delta V_{FWHM}$ (km s^{-1})	H_2 $^{3}\alpha_{\rm H_2}$ (degrees)	$^{4}V_{\rm sys}$ (km s^{-1})	$^{5}\theta$ (degrees)
SVS 13							8	40(±5)
LVC	−35	~67	100	−20	34	86		
IVC				−89	~36	32		
HVC	−133	70	42					
B5-IRS1[6]							10	77(±10)
LVC				4	35	105		
HVC	–	~46	–					
IRAS 04239+2436							8	60(±20)
LVC				7	35	174		
HVC	−125	~57	24					
L1551-IRS5[6]							6	45(±10)
LVC				−7	28	113		
HVC	−120	111	64					
EVC	−285	124	34					
HH 34-IRS[6]							8	68(±5)
LVC				1	16	81		
HVC	−95	~57	23					
HH 72-IRS							20	≥45
LVC				13	24	135		
IVC				−40	39	49		
HVC	−130	~46	24	−129	19	10		
HH 379-IRS							4	–
LVC	0	53	–	4	15	–		

Parameters for the FEL regions (from the [FeII] data) and MHEL regions (H_2 data from Paper I) extracted from the spectra in Fig. 6. The [FeII] and H_2 spectra cover the same effective area on each source, though note that source distances vary, in the range 140 pc to 1.7 kpc (see Table 3).
[1] Velocity of the component peak. This radial velocity is not corrected for the flow inclination angle, nor has the systemic LSR velocity been subtracted.
[2] *FWHM* of the extracted profile, with the instrumental profile deconvolved (i.e. $\Delta V_{FWHM} = \sqrt{(\Delta V^2_{\rm observed} - \Delta V^2_{\rm instrumental})}$.
[3] Opening angle attributed to each individual flow component; $\alpha = 2\arctan(\Delta V_{FWHM} \times \cos\theta / \mid V_{\rm peak} - V_{\rm sys} \mid)$.
[4] Systemic LSR velocity of the region (see text for references).
[5] Inclination angle of the flow with respect to the line of sight (see Paper I for references).
[6] The [FeII] parameters for these sources were measured "by eye" from the spectra, rather than by fitting a Gaussian to the profile.

radial velocities comparable with the rest of the jet further downstream, while the H_2 emission towards the source is only slightly blue-shifted, by a few tens of km s^{-1}, even though higher-velocity H_2 is often detected further downstream (see e.g. HH 34 and L 1551-IRS 5 in Fig. 7). Also, the [FeII] emission peaks are spatially further offset along the jet axes than the H_2 peaks (compare Fig. 4 above with the same graphs in Fig. 4 of Paper I). It therefore seems likely that the [FeII] emission is more closely tied to emission knots and shock fronts along the extended jet axes, while the H_2 is predominantly excited closer to the outflow source in each system, where ambient gas densities rise sharply. The slow-moving H_2 probably derives from the boundary between the jet and the stationary ambient gas.

In Table 2 we compare the line peak velocities and the line widths of the individual velocity components observed in H_2 and [FeII]. From these data we crudely estimate an opening angle, α, for each velocity component, from the velocity of the emission peak and the component width (we assume that the velocity dispersion, $\Delta V = \Delta V_{FWZI} \sim 2 \times \Delta V_{FWHM}$). These data are corrected for outflow inclination angle (where known) and the systemic velocity. The estimated angles are at best only upper limits, since each line component width will be broadened by dynamical processes other than the lateral expansion of the jet (e.g. turbulence, rotation, etc.). Nevertheless, the higher-velocity jet components, seen predominantly in [FeII], are probably more highly collimated than the lower-velocity molecular components seen (in all cases) in H_2, even though the [FeII] profiles are in all cases broader.

In Table 3 we then list integrated line intensities measured from each extracted H_2 and [FeII] spectrum in Fig. 6. From these we are able to estimate a mass outflow rate and momentum for the flow components seen in H_2 and [FeII] respectively. $\dot{M}_{\rm H_2}$ and $MV_{\rm H_2}$ are taken directly from Paper I. $\dot{M}_{\rm [FeII]}$ and $MV_{\rm [FeII]}$ are derived in essentially the same way.

Table 3. Integrated line intensities.

Source	[1]d (pc)	A_v (mags)	[2]$I_{[FeII]}$ (W m^{-2})	[2]$I_{H_2S(1)}$ (W m^{-2})	[3]$\dot{M}_{[FeII]}$ ($M_\odot$ yr^{-1})	[3]$\dot{M}_{H_2}$ ($M_\odot$ yr^{-1})	[4]$MV_{[FeII]}$ ($M_\odot$ km s^{-1})	[4]MV_{H_2} ($M_\odot$ km s^{-1})
SVS 13	220	30	4.2×10^{-18}	3.7×10^{-16}	8.9×10^{-7}	7.0×10^{-7}	1.9×10^{-3}	6.5×10^{-4}
B5-IRS1	350	10	3×10^{-19}	4.9×10^{-17}	9×10^{-9}	1.7×10^{-8}	2×10^{-5}	2.5×10^{-5}
IRAS 04239+2436	140	30						
blue-jet			1.0×10^{-18}	1.7×10^{-17}	2.6×10^{-7}	3×10^{-9}	2.6×10^{-4}	3×10^{-6}
red-jet			4×10^{-19}	–	9.8×10^{-8}	–	1.0×10^{-4}	–
L1551-IRS5	140	18	1.1×10^{-17}	2.1×10^{-16}	1.7×10^{-7}	4.1×10^{-8}	2.1×10^{-4}	2.4×10^{-5}
HH 34-IRS	450	5	7.2×10^{-18}	1.9×10^{-17}	7.0×10^{-8}	3×10^{-9}	2.1×10^{-4}	7×10^{-6}
HH 72-IRS	1500	–	3×10^{-19}	9.4×10^{-17}	$>2\times10^{-9}$	$>5.8\times10^{-7}$	$>3\times10^{-5}$	$>3.7\times10^{-3}$
HH 379-IRS	900	–	1.8×10^{-18}	1.0×10^{-17}	$>2\times10^{-10}$	$>7\times10^{-10}$	$>1\times10^{-6}$	$>3\times10^{-6}$

[1] Distance to each source.
[2] Integrated line intensities measured across all velocity components listed in Table 2 (taken from the spectra in Fig. 6); the values for H_2 are taken from Paper I. Errors on the [FeII] values are of the order of 0.1–0.3 $\times 10^{-18}$ W m^{-2}. $I_{[FeII]}$ and $I_{H_2S(1)}$ are *not* corrected for extinction.
[3] Mass outflow rate, derived using the peak velocity measured in each line (corrected for inclination angle) and the integrated line intensities in Cols. 4 and 5, corrected for the extinction, A_v, in Col. 3.
[4] Momentum, corrected for inclination angle and extinction.

The observed line intensity, $I_{[FeII]}$, is related to the column density of Fe^+ ions in the upper state of the 1.64 μm transition, N_u, by $I_{[FeII]} = N_u h\nu_{ul} A_{ul}/(4\pi)$, where $I_{[FeII]}$ is measured in W m^{-2} ster^{-1}, A_{ul} is the radiative decay rate of the 1.64 μm transition ($A_{ul} = 0.00465\,s^{-1}$; Nussbaumer & Storey 1988) and ν_{ul} is the frequency of the transition. The total column density of hydrogen atoms and ions, N_H, is then given by $N_H = N_u \times (H/Fe)/(f_u f_{Fe+})$, where f_u and f_{Fe+} are the fraction of Fe^+ ions in the upper state and the fraction of Fe that is singly ionised. (Fe/H) is the Fe-to-H abundance ratio; we adopt a solar ratio of 2.14×10^4 (Grevesse & Ander 1989). Hamann et al. (1994) have calculated values of f_u over a range of electron temperatures and densities; they find that f_u is sensitive only to n_e. For $n_e \sim 10^4$ cm^{-3} (close to the critical density for excitation of the observed transition) a value of $f_u = 0.01$ is predicted, which we use here. Hamann (1994) also predict $f_{Fe+} \sim 0.68$ under similar conditions.

The mass outflow rates and momenta in Table 3 are calculated for the areas encompassed by the 3-row-wide extracted spectra displayed in Fig. 6. In the H_2 and [FeII] observations this angular area is the same, though because of the different distances to each region the actual area differs from source to source. In calculating $\dot{M}$ we assume that the emission is extended along the jet axis, i.e. $\dot{M} = M/\tau$, where τ ($\sim L/[V_{peak}\tan\theta]$) is a dynamical time scale for the observed section of the jet. If the emission is unresolved along the jet, τ will be overestimated and $\dot{M}$ will be underestimated, although because we have already established that the emission is offset and/or extended along the axis in each system (in H_2 and [FeII]), this is probably not a dominant source of uncertainty.

The largest sources of error in $\dot{M}$ and MV in Table 3 are probably; (1) the value of A_v used to correct the observed intensities, $I_{[FeII]}$ and I_{H_2}, for extinction, (2) the inclination angle of the flow, and (3) the velocity adopted for the [FeII] and H_2 flow components. The values of A_v used (references are listed in Paper I) are estimated usually from molecular column densities measured from (sub)mm observations made at low angular resolution, or optical line ratios. Clearly, because neither the submm nor the optical emission derives from the same region as the near-IR emission very near to each source, the values of A_v used in our analysis will be uncertain, and probably underestimated (because of beam dilution in the submm, or because the optical emission is detected only from lower-extinction regions further out). Low-resolution H-band spectroscopy would be useful to measure the extinction from the ratio of the [FeII] lines at 1.644 μm and 1.257 μm (e.g. Reipurth et al. 2000). Then the extinction towards the [FeII] region – probably the largest source of error in Table 3 – would be measured directly. In a few sources A_v is not know at all; for HH 72-IRS and HH 379-IRS we do not correct the parameters in Table 3 for extinction, so these are listed as lower limits. An A_v of ~25–40 would result in an increase of the order of 10^2–10^3 in $\dot{M}_{[FeII]}$ and $MV_{[FeII]}$, and 10–40 in $\dot{M}_{H_2}$ and MV_{H_2}. (Note, however, that a very high value of A_v would probably render the [FeII] emission unobservable!)

The inclination angle of the jet in most cases is known to within ~10%, so this is probably a secondary source of uncertainty. The choice of flow velocity used to calculate $\dot{M}$ and MV is, however, somewhat arbitrary. We use the radial velocity of the emission peak, V_{peak}, since we assume that the broad line widths observed (particularly in [FeII]) are largely due to lateral expansion of the flow, turbulence in a shear layer between the jet and the stationary ambient medium, and thermal motions in the post-shock gas. An uncertainty in V_{peak} of 10–50 km s^{-1} could nevertheless result in an additional error in $\dot{M}$ and MV of a factor of 2–3. Overall then, we estimate an approximate error of the order of a factor of 10–100 on the mass loss rates and momenta listed in Table 3.

Even given the uncertainties listed above, the mass-loss rates and momenta in Table 3 are fairly typical of HH jets from low-mass YSOs, where e.g. the average mass loss rates vary from 1×10^{-6} to 5×10^{-8} $M_\odot$ yr^{-1}

(Bacciotti & Eislöffel 1999). In HH 34, for example, which is the most well defined jet in [SII], [FeII] and H_2 emission, a mass-loss rate of $2–4 \times 10^{-7}$ $M_\odot$ yr^{-1} has been measured from optical emission-line studies (Heathcote & Reipurth 1992; Bacciotti & Eislöffel 1999); in [FeII] we derive a mass loss rate at the base of the jet of 7×10^{-8} $M_\odot$ yr^{-1}, which is only a factor of 3–5 lower. And in L 1551-IRS5, a momentum of $<7 \times 10^{-4}$ $M_\odot$ km s^{-1} has been predicted from recent HST observations (Fridlund & Liseau 1998); in [FeII] we estimate $MV_{\rm [FeII]} \sim 2 \times 10^{-4}$ $M_\odot$ km s^{-1}. The mass loss rates and momenta in Table 3 are therefore not unreasonable.

It is also worth noting that, although the absolute errors on $\dot{M}$ and MV for the H_2 and [FeII] flow components may be large, the *relative* errors between these two parameters will be much smaller, because the *same* extinction is used for each data set. Consequently, if the [FeII] traces a collimated jet component, then the above analysis suggests that the momentum in this jet is equal to or greater than the momentum in the more poorly-collimated, molecular outflow which we trace in H_2 in each system. Moreover, given the higher velocities associated with the [FeII] jet component, the momentum supply rate, $\dot{M}V$, of each jet should be sufficient to drive the H_2 flow. In other words, the [FeII] jet will supply enough momentum per unit time to entrain and accelerate the molecular flow seen in H_2. There is even some evidence that this process is more efficient in the more deeply embedded outflows, like SVS 13 and B5-IRS1 (which have no optical jet) than it is in the less-embedded flows, like L 1551-IRS 5 and HH 34-IRS (both YSOs have well-known optical jets observed close to the central engine), since in SVS 13 and B5-IRS1 the momentum in the [FeII] and H_2 components are roughly equal, while in L 1551-IRS 5 and HH 34 $MV_{\rm [FeII]}$ is an order of magnitude greater than $MV_{\rm [H_2]}$.

Finally, we reiterate that there is also some evidence to suggest that the H_2 component is more poorly collimated than the [FeII] jet, as one would expect if the former is entrained in a boundary layer between the jet and the ambient medium. It seems likely, therefore, that entrainment of molecular material is present in YSO jets even within a few hundred AU of the central driving source. Higher-resolution spectroscopy across the width of a few MHEL flows are clearly needed to investigate this possibility further. Moreover, X-wind and disk-wind models should also now strive to predict FEL *and* MHEL characteristics within the first 1000 AU of the central outflow source, since observational data at high spatial and spectral resolution are now forthcoming.

9. Conclusions

[FeII] long-slit echelle spectroscopy of seven Class I YSOs and three CTTSs is presented. We detect emission towards the H-band continuum positions of all seven Class I sources (Fig. 6) and along the extended jet lobes of three of these. [FeII] emission is also detected in the HH jets of the three CTTSs; in RW Aur and DG Tau this emission is traced to within a few arcseconds of the source.

From a comparison of the [FeII] observations with published [SII] observations and the H_2 observations in a companion paper (Paper I) we arrive at the following conclusions:

1. The [FeII] emission is typically blue-shifted to much higher velocities than the H_2 emission in the FEL/MHEL region in each Class I YSO. Where low and high-velocity components are observed in H_2, the [FeII] is usually brightest or even confined to the HVC, while the H_2 emission is strongest in the LVC.
2. The [FeII] emission *peak* is usually offset further along the jet axis (from the source continuum centroid) than the H_2 emission.
3. The [FeII] peak velocities, range of velocities observed and the distribution in [FeII] emission along each jet axis closely follows that seen in [SII], in the Class I YSOs where the latter is observed (e.g. HH 34 and L 1551-IRS5) and in all three CTTS jets.

We suggest that the [FeII] emission derives from the base of a collimated, high-velocity jet which entrains ambient molecular gas within a few hundred AU of each HH energy source. The entrained gas is observed in H_2 emission. Our analysis indicates that the [FeII] jet may well have sufficient power to drive the H_2 flow.

Lastly, Br12 emission was also detected towards the CTTSs and towards two of the Class I YSOs. These HI emission profiles are very broad, though they are single-peaked and relatively symmetric in shape. The profiles peak at low blue-shifted velocities. The emission is also confined to the source position, i.e. we see no distinct offset of the emission peak along the jet axis, and we do not detect Br12 from the extended jet regions. We therefore associate the emission with the same high-excitation regions observed in Brγ in Paper I, namely the inner regions of the accretion disk, magnetospheric accretion flows, and/or the first few AU of the jet.

Acknowledgements. We thank Watson Varricatt for his assistance at the telescope. The *UKIRT* is operated by the Joint Astronomy Centre on behalf of the U.K. Particle Physics and Astronomy Research Council. The Starlink Software Collection is managed and distributed by the Starlink Project which is funded by PPARC.

References

Anglada, G., Rodríguez, L. F., & Torrelles, J. M. 2000, ApJ, 542, L123
Bacciotti, F., & Eislöffel, J. 1999, A&A, 342, 717
Bacciotti, F., Hirth, G. A., & Natta, A. 1996, A&A, 310, 309
Bacciotti, F., Mundt, R., Ray, T. P., et al. 2000, ApJ, 537, L49
Bacciotti, F., Ray, T. P., Mundt, R., Eisloeffel, J., & Solf, J. 2002, ApJ, 576, 222
Bachiller, R., & Cernicharo, J. 1990, A&A, 239, 276
Bachiller, R., Gueth, F., Guilloteau, S., Tafalla, M., & Dutrey, A. 2000, A&A, 362, L33
Bally, J., Devine, D., & Alten, V. 1996, ApJ, 473, 921
Bührke, T., Mundt, R., & Ray, T. P. 1988, A&A, 200, 99
Carr, J. S. 1993, ApJ, 406, 553
Chernin, L. M., & Masson, C. R. 1995, ApJ, 443, 181
Chrysostomou, A., Hobson, J., Smith, M. D., Davis, C. J., & Berndsen, A. 2000, MNRAS, 314, 229

Curiel, S., Raga, A., Raymond, J., Noriega-Crespo, A., & Cantó, J. 1997, AJ, 114, 2736
Davis, C. J., Eislöffel, J., & Smith, M. D. 1996, ApJ, 463, 246
Davis, C. J., Mundt, R., Ray, T. P., & Eislöffel, J. 1995, AJ, 110, 766
Davis, C. J., Ray, T. P., Desroches, L., & Aspin, C. 2001, MNRAS, 326, 524 (Paper I)
Davis, C. J., Ray, T. P., Eislöffel, J., & Corcoran, D. 1997, A&A, 324, 263
Davis, C. J., Stern, L., Ray, T. P., & Chrysostomou, A. 2002, A&A, 382, 1021
Devine, D., Bally, J., Reipurth, B., & Heathcote, S. 1997a, AJ, 114, 2095
Devine, D., Reipurth, B., & Bally, J. 1997b, in Low-mass star formation – from infall to outflow, poster Proc., ed. F. Malbet, & A. Castets, IAU Symp., 182, 91
Dobashi, K., Bernard, J.-P., Yonekura, Y., & Fukui, Y. 1994, ApJS, 95, 419
Dougados, C., Cabrit, S., Lavalley, C., & Ménard, F. 2000, A&A, 357, L61
Edwards, S., & Snell, R. L. 1982, ApJ, 261, 151
Eislöffel, J., Günther, E., Hessman, F. V., et al. 1991, ApJ, 383, L19
Eislöffel, J., & Mundt, R. 1992, A&A, 263, 292
Eislöffel, J., & Mundt, R. 1997, AJ, 114, 280
Eislöffel, J., Solf, J., & Böhm, K. H. 1990, A&A, 237, 369
Everett, M. E., De Poy, D. L., & Pogge, R. W. 1995, AJ, 110, 1295
Folha, D. F. M., & Emerson, J. P. 2000, A&A, 365, 90
Fridlund, C. V. M., & Liseau, R. 1998, ApJ, 499, L75
Gahm, G. F., Petrov, P. P., Duemmler, R., Gameiro, J. F., & Lago, M. T. V. T. 1999, A&A, 352, L95
Garden, R. P., Russell, A. P. G., & Burton, M. G. 1990, ApJ, 354, 232
Gredel, R. 1996, A&A, 305, 582
Greene, T. P., & Lada, C. J. 1996, ApJ, 461, 345
Grevesse, N., & Anders, E. 1989, in Cosmic Abundances of Matter, ed. C. I. Waddington (New York: AIP), AIOP Conf. Proc., 183, 1
Hamann, F. 1994, ApJS, 93, 485
Hamann, F., Simon, M., Carr, J. S., & Prato, L. 1994, ApJ, 436, 292
Hartigan, P., Morse, J., Palunas, P., Bally, J., & Devine, D. 2000, ApJ, 119, 1872
Hartigan, P., Mundt, R., & Stocke, J. 1986, AJ, 91, 1357
Hartigan, P., Raymond, J. C., & Hartmann, L. 1987, ApJ, 316, 323
Hartmann, L., Hewett, R., & Calvet, S. 1994, ApJ, 426, 669
Heathcote, S., & Reipurth, B. 1992, AJ, 104, 2193
Hirth, G., Mundt, R., & Solf, J. 1997, A&AS, 126, 437
Hirth, G., Mundt, R., Solf, J., & Ray, T. P. 1994, ApJ, 427, L99
Hollenbach, D., & McKee, C. F. 1989, ApJ, 342, 306
Hummer, D. G., & Storey, P. J. 1987, MNRAS, 224, 801
Itoh, Y., Kaifu, N., Hayashi, M., et al. 2000, PASJ, 52, 81
Johansson, S. 1978, Phys. Scr., 18, 217
Khanzadyan, T., Smith, M. D., Davis, C. J., et al. 2002, MNRAS, in press
Kitamura, Y., Kawabe, R., & Saito, M. 1996, ApJ, 457, 277
Lavalley, C., Cabrit, S., Dougados, C., Ferruit, P., & Bacon, R. 1997, A&A, 327, 671
Luhman, K. L., & Rieke, G. H. 1996, ApJ, 461, 298
Maihara, T., Iwamuro, F., Yamashita, T., et al. 1993, PASP, 105, 940
Moriarty-Schieven, G., & Snell, R. L. 1988, ApJ, 332, 364
Mountain, C. M., Robertson, D., Lee, T. J., & Wade, R. 1990, in Instrumentation in Astronomy, SPIE 1235, VII, 25
Mundt, R., Brugel, E. W., & Bührke, T. 1987, ApJ, 319, 275
Mundt, R., & Eislöffel, J. 1998, AJ, 116, 860
Mundt, R., & Fried, J. 1983, ApJ, 274, L83
Mundt, R., Ray, T. P., & Raga, A. C. 1991, A&A, 252, 740
Mundt, R., Stocke, J., & Stockman, H. S. 1983, ApJ, 265, L71
Muzerolle, J., Calvet, N., & Hartmann, L. 1998, ApJ, 116, 2965
Nussbaumer, H., & Storey, P. J. 1988, A&A, 193, 327
Pyo, T.-S., Hayashi, M., Kobayashi, N., et al. 2002, ApJ, 570, 724
Ray, T. P., Mundt, R., Dyson, J. E., Falle, S. A. E. G., & Raga, A. C. 1996, ApJ, 468, L103
Rieke, G. H., & Lebovsky, M. J. 1985, ApJ, 288, 618
Reipurth, B., Bally, J., & Devine, D. 1997, AJ, 114, 2708
Reipurth, B., & Graham, J. A. 1988, A&A, 202, 219
Reipurth, B., Pedrosa, A., & Lago, M. T. V. T. 1996, A&AS, 120, 229
Reipurth, B., Yu, K. C., Heathcote, S., Bally, J., & Rodríguez, L. 2000, AJ, 120, 449
Schwartz, R. D., Gee, G., & Huang, Y.-L. 1988, ApJ, 327, 350
Shu, F. H., Ruden, S. P., Lada, C. J., & Lizano, S. 1991, ApJ, 370, L31
Shu, F. H., Najita, J., Ostriker, E. C., & Shang, H. 1995, ApJ, 455, L155
Shu, F. H., Najita, J., Shang, H., & Li, Z. Y. 2000, in Protostars and Planets IV, ed. V. Mannings, A. P. Boss, & S. S. Russell (Tucson: Univ. Arizona Press), 789
Shull, J. M., & Hollenbach, D. J. 1978, ApJ, 220, 525
Solf, J., Böhm, K. H., & Raga, A. 1986, ApJ, 305, 795
Stapelfeldt, K. R., Scoville, N. Z., Beichman, C. A., Hester, J., & Gautier, T. N. 1991, ApJ, 371, 226
Stocke, J. T., Hartigan, P., Strom, S. E., et al. 1988, ApJS, 68, 229
Takami, M., Chrysostomou, A., Bailey, J., et al. 2002, ApJ, 568, L53
Takami, M., Bailey, J., Gledhill, T. M., Chrysostomou, A., & Hough, J. H. 2001, MNRAS, 323, 177
Ungerechts, H., & Thaddeus, P. 1987, ApJS, 63, 645
Woitas, J., Ray, T. P., Bacciotti, F., Davis, C. J., & Eislöffel, J. 2002, ApJ, in press
Yu, K. C., Billawala, Y., & Bally, J. 1999, ApJ, 118, 2940